

**Involvement of N-type voltage dependent calcium  
channels in axon degeneration during experimental  
autoimmune optic neuritis**

Dissertation  
zur Erlangung des Doktorgrades  
der Mathematisch-Naturwissenschaftlichen Fakultäten  
der Georg-August-Universität

vorgelegt von  
**Ivana Gadjanski**  
aus Novi Sad, Serbien

Göttingen 2007

D 7

Referent: Herr Prof. Dr. R. Hardeland

Korreferent: Herr Prof. Dr. R. Heinrich

Tag der mündlichen Prüfung: 31.10.2007

## Declaration

**This thesis has been written independently and with no other sources and aids than stated and presents a description of my own work.**

**Ivana Gadjanski**

**Date** \_\_\_\_\_

**Signature** \_\_\_\_\_

**За маму и тату**

*To my parents*

<b>1</b>	<b>ABSTRACT</b>	<b>7</b>
<b>2</b>	<b>INTRODUCTION</b>	<b>9</b>
	2.1. Multiple sclerosis – pathological features and pathogenesis	9
	2.2. General mechanisms of injury and repair in MS	10
	2.3. Patterns of demyelination in MS	12
	2.4. Axonal damage in MS	14
	2.5. Myelin oligodendrocyte glycoprotein (MOG) – induced experimental autoimmune encephalomyelitis (EAE)	17
	2.6. Voltage dependent calcium channels – structure, function, distribution and classification (VDCC)	19
	2.7. VDCCs as therapeutic targets	23
	2.8. Magnetic resonance imaging (MRI) for visualization of MS and EAE pathology	25
	2.9. Manganese enhanced MRI	26
	<b>AIM OF THE STUDY</b>	<b>27</b>
<b>3</b>	<b>METHODS</b>	<b>28</b>
	3.1. Animals	28
	3.2. Immunogen	28
	3.3. Induction and evaluation of EAE	28
	3.4. Retrograde labeling of RGCs	29
	3.5. Quantification of RGC density	29
	3.6. Optic nerve histopathology	29
	3.7. Immunohistochemistry	30
	3.8. Experimental setup for manganese enhanced MRI	32
	3.9. Analysis of MR images	34
	3.10. Labeling of the optic nerve with a calcium sensitive dye	35
	3.11. <i>In vivo</i> calcium imaging	35
	3.12. Intracerebroventricular infusion	36
	3.13. Statistical analysis	37
<b>4</b>	<b>RESULTS</b>	<b>38</b>
	4.1. In optic neuritis signal intensity in T1-weighted MR images is reduced and Mn <sup>2+</sup> - induced enhancement is prominent	38
	4.2. High voltage-activated calcium channels mediate Mn <sup>2+</sup> - induced enhancement	39
	4.3. Mn <sup>2+</sup> enters the inflamed ON via N-type VDCCs	40
	4.4. N-type VDCC expression is up-regulated in optic neuritis and correlates with demyelination pattern	42
	4.5. N-type VDCC expression correlates with immunoreactivity for $\beta$ -amyloid precursor protein	46

	4.6. Expression of N-type VDCC in optic neuritis does not correlate with CNPase reactivity	47
	4.7. $\omega$ -conotoxin GVIA suppresses $\text{Ca}^{2+}$ influx into the inflamed ON	48
	4.8. Application of $\omega$ -conotoxin GVIA reduces axonal degeneration in MOG-induced optic neuritis	50
<b>5</b>	<b>DISCUSSION</b>	<b>55</b>
	5.1. Detection of N-type VDCC expression pattern in MOG-induced optic neuritis	55
	5.2. Establishing functionality of the ectopically expressed N-type VDCC	57
	5.3. Therapeutic value of $\omega$ -conotoxin GVIA, advantages and negative side-effects	58
	5.4. Effects of intracerebroventricular continuous infusion of $\omega$ -conotoxin GVIA on MOG-induced optic neuritis	59
	5.5. Hypothetical mechanism of N-type VDCC up-regulation in MOG-immunized optic nerve	61
<b>6</b>	<b>CONCLUSIONS</b>	<b>63</b>
<b>7</b>	<b>REFERENCES</b>	<b>65</b>
	<b>LIST OF TABLES AND FIGURES</b>	<b>76</b>
	<b>APPENDIX 1: Abbreviations</b>	
	<b>APPENDIX 2: CV</b>	
	<b>ACKNOWLEDGMENTS</b>	<b>84</b>

## 1 Abstract

Optic neuritis is one of the most common clinical manifestations of multiple sclerosis (MS), a chronic inflammatory disease of the central nervous system (CNS). After an episode of optic neuritis, 30–50 % of patients develop persistent impairment of vision caused by degeneration of optic nerve (ON) axon fibers. Our group has previously shown that in Brown Norway (BN) rats, myelin oligodendrocyte glycoprotein (MOG) – induced experimental autoimmune encephalomyelitis (EAE) affects the optic nerve in more than 90% of immunized animals, leading to inflammation, demyelination, and degeneration of axons. The precise pathological mechanisms of axonal degeneration are not fully understood, but are likely to involve excess accumulation of calcium ions ( $\text{Ca}^{2+}$ ) into axons. One of the possible routes of entry of  $\text{Ca}^{2+}$  under pathological conditions is via different types of voltage-dependent calcium channels (VDCCs). Since manganese ions ( $\text{Mn}^{2+}$ ) also enter neurons via VDCCs and cause signal enhancement in T1-weighted magnetic resonance images (MRI), we have used  $\text{Mn}^{2+}$ -enhanced MRI to evaluate the effects of type specific VDCC blockers.

We found that application of  $\omega$  – conotoxin GVIA, a specific blocker of N-type VDCCs, caused a significant decrease of  $\text{Mn}^{2+}$ - induced enhancement in T1-weighted MR images. In order to further investigate N-type VDCC expression in the ON, we have performed immunohistochemistry for  $\alpha_{1B}$ , the pore-forming subunit of N-type VDCCs, which revealed a significant difference in both the degree and the pattern of N-type VDCC expression between healthy and inflamed ONs. In healthy, myelinated ONs, a modest degree of  $\alpha_{1B}$  immunoreactivity was detected. However, a highly significant up-regulation of expression was seen in MOG-immunized ONs. Furthermore, a highly significant positive correlation between the number of  $\alpha_{1B}$ -positive sites per ON and the percentage of demyelination was detected by myelin-specific histopathological staining. A highly significant negative correlation was observed between the number of  $\alpha_{1B}$ -positive sites per ON and the percentage of axonal survival.

Additionally, we have tested the N-type VDCC blocker,  $\omega$  – conotoxin GVIA, during an *in vivo* calcium imaging study. After  $\omega$ -conotoxin GVIA was topically applied to the inflamed ONs, depolarization-induced influx of  $\text{Ca}^{2+}$  was significantly inhibited in comparison to the control group of MOG-immunized ONs. Treatment of healthy rats with the N-type VDCC blocker decreased the  $\text{Ca}^{2+}$  signal to a smaller extent which

was not significantly different to healthy ONs after topical application of normal saline. These results confirm the previously obtained data about up-regulated expression of N-type VDCCs in MOG-immunized ONs and indicate further that the newly expressed N-type VDCCs are functional.

Taken together, our data indicate N-type VDCCs to have the most prominent effect on  $\text{Ca}^{2+}$  influx in MOG-induced optic neuritis. Further corroboration was acquired by showing therapeutically significant effects of a specific N-type VDCC blocker,  $\omega$ -conotoxin GVIA, after intracerebroventricular continuous infusion. We detected significantly decreased demyelination and a significant increase of axonal survival in the ONs of  $\omega$ -conotoxin GVIA-treated animals.

Thus, our data show an ectopic expression of N-type VDCCs in MOG-induced optic neuritis in BN rats, which mainly contribute to an increased  $\text{Ca}^{2+}$  influx under autoimmune inflammatory conditions. Furthermore, we introduce  $\omega$ -conotoxin GVIA as a neuroprotective agent in the treatment of autoimmune optic neuritis.

## 2 Introduction

### 2.1. Multiple sclerosis – pathological features and pathogenesis

Multiple sclerosis (MS) is an autoimmune inflammatory and demyelinating disease of the central nervous system (CNS). In the last years, however, it has become increasingly apparent that neurodegeneration plays an important role in MS and is the key factor of chronic disability (Trapp, 1999). A number of recent studies showed either by histopathology and magnetic resonance imaging (MRI) (Kornek, 2000; Losseff, 1996) or by using animal models (Meyer, 2001; Diem, 2003; Hobom, 2004) that axonal and neuronal damage starts in the earliest stages of the disease. However, the exact sequence of events which leads to disease development is largely unknown. There are several reasons for this. First of all, multiple sclerosis is rather a complex of syndromes with different causes and pathogenic mechanisms than a single disease (Noseworthy, 2000), which is reflected by a significant degree of clinical, genetic, MRI and pathological heterogeneity described for MS (Lucchinetti, 2000). The diversity of MS etiology and symptoms requires different therapeutic approaches in order to treat the specific disease type effectively (Table 1).

However, there are pathological hallmarks which distinguish MS from other inflammatory CNS diseases. These are, namely, large, multifocal, demyelinated plaques with reactive glial scar formation (Lassmann, 2001). This demyelinating process is accompanied by an inflammatory reaction with infiltrates composed mainly of T-cells and macrophages. Myelin sheaths and oligodendrocytes (OG) can be destroyed, possibly by different mechanisms in different individuals, which results in distinctly different patterns of demyelination in active lesions. Lesions are predominantly formed in the optic nerves, periventricular white matter, brain stem, cerebellum and spinal cord white matter, and they often surround one or several medium-sized vessels (Noseworthy, 2000).

<b>MS types</b>	<b>Current treatment agents</b>
<b>Relapsing-remitting</b>	<b>Interferon beta-1b, Interferon beta-1a, Glatiramer acetate, Immunoglobulins</b>
<b>Secondary progressive</b>	<b>Interferon beta-1b, Mitoxantrone hydrochloride</b>
<b>Primary progressive</b>	<b>None</b>
<b>Acute relapses</b>	<b>Corticosteroides, plasma exchange</b>

**Table 1: Classification of MS types and current treatments.**

Modified from Noseworthy, 2000

## **2.2. General mechanisms of injury and repair in MS**

MS is generally considered to be an autoimmune disease that is induced when T helper 1 (Th1) cells recognize components of the myelin sheath (Lucchinetti, 2000). However, this is an oversimplified description of the events which lead to the pathologies described in different types of MS. Another important aspect to consider is the effect of genetic and environmental factors on susceptibility to MS. These factors include viral infection, bacterial lipopolysaccharides, superantigens, reactive metabolites, and metabolic stress and may facilitate the movement of autoreactive T cells and demyelinating antibodies from the systemic circulation into the CNS through disruption of the blood–brain barrier (BBB). In the CNS, local factors (including viral infection and metabolic stress) may up-regulate the expression of endothelial adhesion molecules, such as intercellular adhesion molecule 1 (ICAM-1), vascular-cell adhesion molecule 1 (VCAM-1), and E-selectin, further facilitating the entry of T cells into the CNS. Proteases, including matrix metalloproteinases, may further enhance the migration of autoreactive immune cells by degrading extracellular-matrix macromolecules. Pro-inflammatory cytokines released by activated T cells, such as interferon- $\gamma$  and tumor necrosis factor- $\alpha$  (TNF-  $\alpha$ ), may up-regulate the expression of cell-surface molecules on neighbouring lymphocytes and antigen-presenting cells. Binding of putative MS antigens, such as myelin basic protein, myelin-associated glycoprotein, myelin oligodendrocyte glycoprotein (MOG), proteolipid protein,  $\alpha$ B-crystallin, phosphodiesterases, and S-100 protein, by the trimolecular complex — the

T-cell receptor (TCR) and class II major-histocompatibility-complex (MHC) molecules on antigen-presenting cells — may trigger either an enhanced immune response against the bound antigen or anergy, depending on the type of signaling that results from interactions with surface co-stimulatory molecules (e.g., CD28 and CTLA-4) and their ligands (e.g., B7-1 and B7-2). Down-regulation of the immune response (anergy) may result in the release of anti-inflammatory cytokines (interleukin-1, interleukin-4, and interleukin-10) from CD4+ T cells, leading to the proliferation of anti-inflammatory CD4+ type 2 helper T (Th2) cells. Th2 cells may send anti-inflammatory signals to the activated antigen-presenting cells and stimulate pathologic or repair-enhancing antibody-producing B cells. Alternatively, if antigen processing results in an enhanced immune response, pro-inflammatory cytokines (e.g., interleukin-12 and interferon- $\gamma$ ) may trigger a cascade of events, resulting in the proliferation of pro-inflammatory CD4+ type 1 helper T (Th1) cells and ultimately in immune-mediated injury to myelin and oligodendrocytes. Multiple mechanisms of immune-mediated injury of myelin have been postulated: cytokine-mediated injury of oligodendrocytes and myelin, digestion of surface myelin antigens by macrophages, including binding of antibodies against myelin and oligodendrocytes (i.e. antibody-dependent cytotoxicity), complement-mediated injury, and direct injury of oligodendrocytes by CD4+ and CD8+ T cells. This injury to the myelin membrane results in denuded axons that are no longer able to transmit action potentials efficiently within the CNS (loss of saltatory conduction). This slowing or blocking of the action potential produces neurologic symptoms. The exposed axon segments may be susceptible to further injury from soluble mediators (including cytokines, chemokines, complement, and proteases), resulting in irreversible axonal injury (such as axonal transection and terminal axon ovoids).

There are several possible mechanisms of repair of the myelin membrane, including resolution of the inflammatory response followed by spontaneous remyelination, spread of sodium channels from the nodes of Ranvier to cover denuded axon segments and restore conduction, antibody-mediated remyelination, and remyelination resulting from the proliferation, migration, and differentiation of resident oligodendrocyte precursor cells. The described events and possible mechanisms are depicted in Figure 2.1.

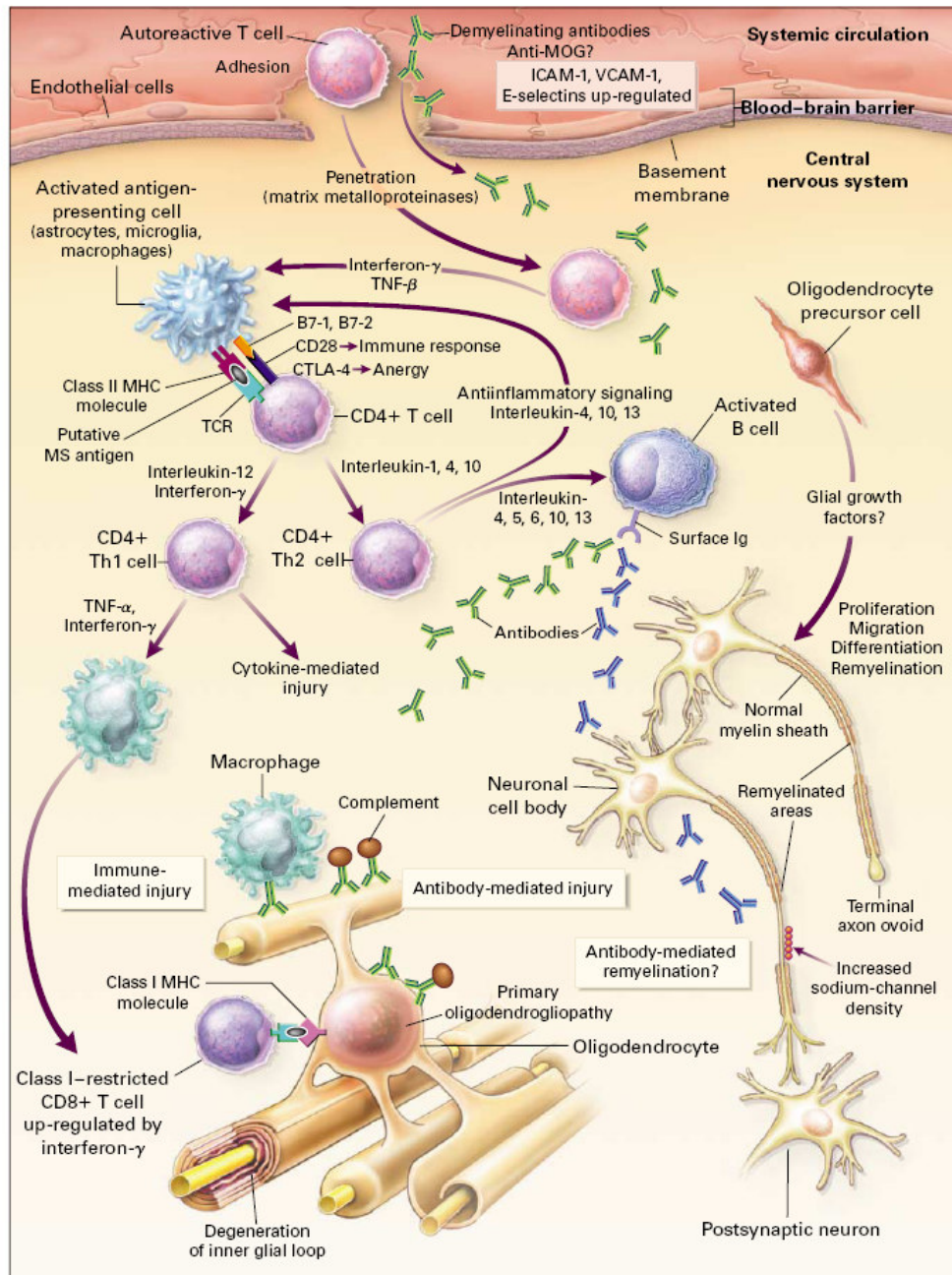


**Fig.2.1: Possible mechanisms of injury and repair in multiple sclerosis** (detailed explanation given in the text). Scheme taken from Noseworthy, 2000

### 2.3. Patterns of demyelination in MS

Demyelination may be induced by macrophages (M) and/or their toxic products (resulting in pattern I), by specific demyelinating antibodies and complement (C,

resulting in pattern II), by degenerative changes in distal processes, in particular those of periaxonal oligodendrocytes (distal oligodendrogliopathy), followed by apoptosis (resulting in pattern III) or by a primary degeneration of oligodendrocytes followed by myelin destruction (resulting in pattern IV). Most prominent characteristics of pathology of different MS patterns of demyelination as well as putative mechanisms are summarized in the Table 2.

Patterns of demyelination	Pathology	Putative mechanisms
<p>Pattern I Macrophage-mediated demyelination</p>	<p>Perivenous distribution and radial expansion of lesions; inflammatory infiltrates composed of T-cells and macrophages</p>	<p>T-cell mediated inflammation with macrophage/microglia activation, demyelination induced by macrophage toxins</p>
<p>Pattern II Antibody-mediated demyelination</p>	<p>Similar lesions as in I but additional deposition of immunoglobulin and activated complement at sites of active myelin destruction</p>	<p>T-cell mediated inflammation with macrophage/microglia activation, complement mediated lysis of antibody-targeted myelin</p>
<p>Pattern III Distal oligodendrogliopathy &amp; apoptosis</p>	<p>Inflammation by T-cells and macrophages, small vessel vasculitis with endothelial cell damage and microvessel thrombosis, degeneration of distal oligodendrocyte processes, followed by oligodendrocyte apoptosis and demyelination</p>	<p>T-cell mediated small vessel vasculitis with secondary ischemic damage of the white matter</p>
<p>Pattern IV Primary oligodendroglia degeneration</p>	<p>Similar lesion as in (I), but prominent oligodendrocyte degeneration in a small rim of periplaque white matter</p>	<p>T-cell mediated inflammation with macrophage/microglia activation, demyelination induced by macrophage toxins on the background of metabolically impaired oligodendrocytes; possible genetic defect of oligodendrocytes</p>

**Table 2: Summary of pathologies and putative mechanisms of different patterns of demyelination in MS.** Adapted from Lucchinetti, 2000.

## 2.4. Axonal damage in MS

Axonal pathology has been noted in the earliest pathological descriptions of MS and its cause and functional consequences have been discussed in detail in the early 20th century (Kornek, 1999; Trapp, 1999). However, when it became clear from experimental studies that an inflammatory demyelinating disease similar to MS can be induced by autoimmunity against myelin antigens, the interest in axonal injury vanished. It re-appeared after recent MRI investigations provided increasing evidence for axonal and neuronal loss in MS (Kornek, 1999). These observations suggested that acute axonal injury occurs during a small time window of about two weeks after onset of demyelination (Lassmann, 2003). In addition, there is a slow burning, ongoing axonal destruction, which can be seen even in inactive demyelinated plaques, in which inflammation is sparse or absent. Such ongoing axonal injury is lacking in remyelinated shadow plaques (Kornek, 2000). These data, taken together, suggest that axons in MS lesions are destroyed in two different ways:

During acute demyelination, high numbers of axons are damaged, most likely by the action of toxic inflammatory mediators. This phase of massive axonal injury, however, lasts only for a few days to weeks. In contrast, a low grade of axonal degeneration occurs in silent inactive plaques. Although only few axons are destroyed at a given time point, such lesions may persist in the CNS for years. Thus, this low burning axonal injury may account more to the global axonal loss in MS than axonal degeneration in acute plaques and it may in part also explain the slow progression of clinical disability in the chronic progressive phase of the disease.

When considering the molecular mechanisms of axonal damage, two different phases of axonal disintegration have to be distinguished: the trigger of axonal damage and the downstream pathways of axonal dissolution (Lassmann, 2003). Although the triggers of axonal injury seem to be specific for inflammatory conditions, such as MS, the downstream mechanisms of axonal dissolution appear similar in a variety of different pathological conditions of the nervous system, including inflammation, ischemia, or trauma (Stys, 2004).

Axonal injury can be initiated through direct T cell mediated cytotoxicity. Even more important compared with direct T cell mediated cytotoxicity seems to be the interaction of activated macrophages or microglial cells with axons in the course of axonal injury. Such cells are consistently found in close contact with degenerating

axons. Many of their toxic effector molecules may lead to axonal injury, although a direct injurious effect has so far only been shown for proteases and reactive nitrogen species (Linington, 1993). In particular, nitric oxide (NO) intermediates are particularly attractive candidates. At low concentration, they may induce a functional conduction block, thus explaining clinical deficit in the absence of overt structural damage. At higher concentrations, and in particular when axons are electrically active, NO derivatives may lead to irreversible destruction of axons (Redford, 1997). This may in part be accomplished by the blockade of mitochondrial function and the disturbance of energy metabolism, which can be induced by NO radicals.

In addition to toxins produced by T cells and macrophages, specific antibodies may be involved in the initiation of axonal injury (Lassmann, 2003). The trigger activates several downstream events, which in a cascade of action result in the final dissolution of the axon. The precise mechanisms of axonal degeneration initiated by mentioned triggers under autoimmune inflammatory conditions are not fully understood, but are likely to involve excess accumulation of calcium ( $\text{Ca}^{2+}$ ) ions in the axons (Stys, 2004). Indeed, there has been an increasing number of studies which emphasize the involvement of  $\text{Ca}^{2+}$  in axonal degeneration in trauma (George, 1995), anoxia (Waxman, 1994; Imaizumi, 1999) ischemia (Brown, 2000; Stys, 2005), or inflammatory models (Kornek, 2001).

Under pathological conditions,  $\text{Ca}^{2+}$  may enter the axon via ion-specific transport mechanisms such as voltage-dependent calcium channels (VDCC) and/or reverse operation of the  $\text{Na}^+/\text{Ca}^{2+}$  exchanger (Stys, 1998). Further sequence of events initiated by increased intracellular  $\text{Ca}^{2+}$  concentration would include the activation of calpains and other neutral proteases which could lead to degradation of cytoskeletal components (Banik, 1992).

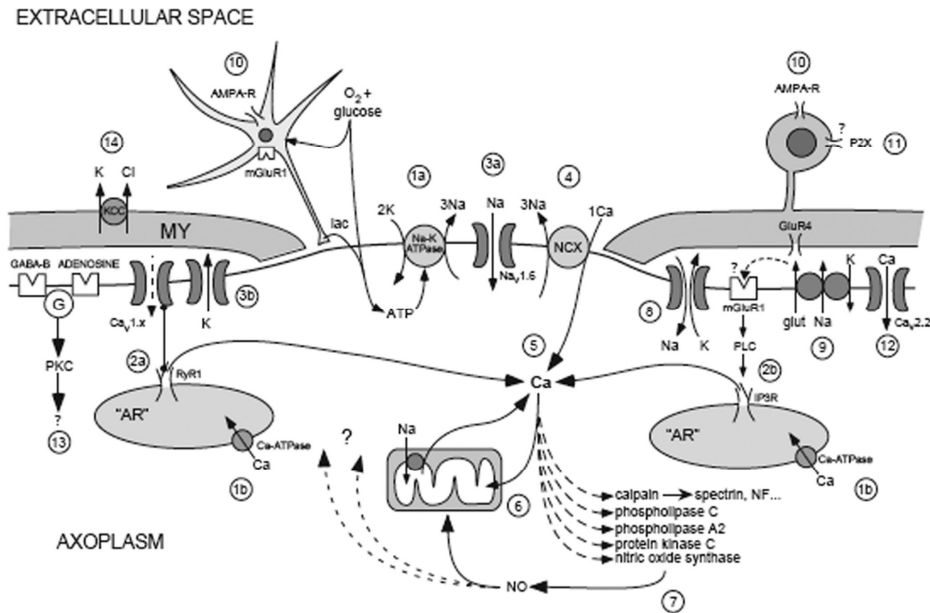


**Fig.2.2: Events initiated during acute injury of CNS white matter**

The locations of the various channels and transporters are drawn for convenience and do not necessarily reflect actual distributions (detailed explanation given in the text). Scheme taken from Stys, 2005.

Disturbance of axoplasmic membrane permeability and a state of relative energy failure leads to uncontrolled ion influx into the axoplasm, in particular in those that are still electrically active (Lassmann, 2003). This creates an energy deficit and/or an excess demand of energy which in turn disturbs the ATP-dependent  $\text{Na}^+ - \text{K}^+$  ATPase (1a) and the  $\text{Ca}^{2+} - \text{ATPase}$  (1b), including those located on the “axoplasmic reticulum” (“AR”). Internal stores of  $\text{Ca}^{2+}$  may contribute significantly to axonal  $\text{Ca}^{2+}$  accumulation, triggered by depolarization via L-type VDCCs (2a) and/or generation of inositol triphosphate (IP3) (2b). The rise in flux through non-inactivating  $\text{Na}^+$ -channels (3a) will increase  $[\text{Na}]_i$  and, together with depolarization caused by  $\text{K}^+$  efflux through a variety of  $\text{K}^+$  channels (3b), stimulates the  $\text{Na}^+ - \text{Ca}^{2+}$  exchanger to operate in the reverse  $\text{Ca}^{2+}$  import mode (4). This  $\text{Ca}^{2+}$  accumulation (5) promotes destructive events including mitochondrial  $\text{Ca}^{2+}$  overload (especially during reoxygenation) (6), and over-activation of several  $\text{Ca}^{2+}$ -dependent enzyme systems (7). Nitric oxide (NO) will inhibit mitochondrial respiration and alter other cellular proteins. Some  $\text{Na}^+$  influx may occur through  $\text{Na}^+/\text{K}^+$  permeable inward rectifier

channels (8). Glutamate is also released through a reversal of  $\text{Na}^+$ -dependent glutamate transport (9), causing cellular injury from activation of ionotropic glutamate receptors (10). Recently, ATP-activated P2X purinergic receptors were suggested to cause  $\text{Ca}^{2+}$ -dependent oligodendroglial injury (11) (Stys, 2005). A component of  $\text{Ca}^{2+}$  influx into damaged axons directly through VDCCs is also likely (12). GABA and adenosine release may play an “autoprotective” role (13). Anion transporters such as the  $\text{K}^+$ - $\text{Cl}^-$  co-transporter participate in volume dysregulation of glial cells and the myelin sheath, contributing to conduction abnormalities (14). (Stys, 2005) However, knowledge concerning the mechanisms of  $\text{Ca}^{2+}$  up-take was mainly derived from investigations in hypoxia models (Stys 2004, 2005) or studies on isolated optic nerve tissue in vitro (Stys, 1993; Waxman, 1994). The relevance of these findings for neurodegeneration under autoimmune inflammatory conditions has been hypothesized rather than it has been formally proven.

## **2.5. Myelin oligodendrocyte glycoprotein (MOG) – induced experimental autoimmune encephalomyelitis (EAE)**

Experimental autoimmune encephalomyelitis (EAE) is the principal model of MS (Wekerle, 1994). Firstly, it was regarded to be a prototypic T cell - mediated autoimmune disease model induced by active immunization with CNS tissue homogenates or purified myelin antigens (Stefferl, 1999). However, nowadays, a whole spectrum of EAE models can be induced by the use of different agents and modes of immunization in susceptible animal strains. In fact, the influence of the major histocompatibility complex genes (MHC) in determining susceptibility to autoimmune diseases was first described for experimental autoimmune encephalomyelitis (EAE) (Stefferl, 1999).

The mechanism by which MHC genes modulate susceptibility to autoimmune diseases is generally discussed in terms of the effects of class I and II MHC alleles on the selection, activation, or effector function of the T cell repertoire (Alberts, 1994). However, this interpretation is derived almost solely from EAE models in which disease is T cell mediated and is independent of the B cell response (Stefferl, 1999). In contrast, human diseases such as MS are generally far more complex in that both cellular and humoral immune effector mechanisms are involved in disease pathogenesis (Noseworthy, 2000). This complex immunopathology is reproduced in

rats with EAE induced by active immunization with the myelin oligodendrocyte glycoprotein (MOG) (Meyer, 2001). MOG is a unique myelin autoantigen in that it induces both an encephalitogenic T cell response and a demyelinating autoantibody response in rodents and primates (Stefflerl, 1999). In the Lewis rat, the T cell response to MOG is only weakly encephalitogenic, and disease induction exhibits an absolute requirement for the MOG-specific autoantibody response. The formation of demyelinating lesions depends on a synergy between the MOG-specific T cell and autoantibody responses (Stefflerl, 1999). The T cell response initiates a subclinical inflammatory reaction in the CNS, disrupting the blood-brain barrier and allowing antibodies to enter the CNS compartment. Activation of the complement cascade by MOG-specific antibodies bound to the myelin surface then initiates demyelination while at the same time enhancing the local inflammatory response through the production of pro-inflammatory factors. The degree of axonal pathology as well as the demyelination pattern in MOG-EAE resembles the one of the human disease (Linington, 1993; Kornek, 2000). Hence, MOG-EAE appears to be one of the most effective animal models for the investigation of both clinical and pathological features of MS (Kornek, 2001).

The brown Norway (BN) rat strain is specifically interesting as a target strain for MOG-induced EAE, given that this rat strain exhibits a generalized resistance to many purely T cell-mediated autoimmune diseases but is susceptible to autoantibody-mediated diseases. Our group has previously demonstrated that in MOG-EAE in BN rats, severe optic neuritis occurs in 80–90% of the animals (Meyer, 2001). Further, we have shown that optic neuritis in this model leads to acute axonal degeneration of the optic nerve (ON) and consecutive apoptosis of retinal ganglion cells (RGCs) (Diem, 2005; Hobom, 2004). The additional advantage is the possibility of a separate evaluation of disease - related effects in the neuronal cell bodies, RGCs, and their associated axons which comprise the optic nerve, due to the anatomical organization of the visual system.

## 2.6. Voltage dependent calcium channels (VDCCs) – structure, function, distribution and classification

Voltage dependent calcium channels (VDCC) mediate calcium influx in response to membrane depolarization in many different cell types. Besides being central to the function of all excitable cells, VDCCs are also crucial in many non-excitable cells (Catterall, 2005). Their activity is essential to couple electrical signals on the cell surface to physiological events in cells. These events include both intracellular processes that either directly utilize elevations of intracellular  $\text{Ca}^{2+}$  concentration as a functional trigger (e.g. exocytosis, muscle contraction) or are modulated by  $\text{Ca}^{2+}$  - dependent signalling cascades (e.g. gene expression, cell division) (Randall, 1999). A detailed overview of the cellular functions and localizations of different VDCC types is given in the Table 3.

Multiple VDCC types with different biophysical and pharmacological characteristics have been described. Until recently, they have been classified into L, N, and P/Q-types, as high voltage activated (HVA) VDCCs, T-type as low voltage activated (LVA), and R-type as intermediate voltage activated (IVA) VDCCs. An alternative classification was made with respect to the pore-forming subunit ( $\alpha_1$ ). L-type VDCCs were referred to channels with  $\alpha_{1C}$ ,  $\alpha_{1D}$ ,  $\alpha_{1F}$  or  $\alpha_{1S}$  pore-forming subunits, N-type VDCCs contain  $\alpha_{1B}$ , P/Q-type VDCCs have  $\alpha_{1A}$  pore-forming subunits and T-type VDCCs contain  $\alpha_{1G}$ ,  $\alpha_{1H}$  or  $\alpha_{1I}$  pore-forming subunits. R-type VDCCs have the  $\alpha_{1E}$  pore – forming subunit of the channel (Bean 1989; Westenbroek, 1992).

However, molecular cloning and biochemical studies showed that this classification does not represent in full the whole complexity of VDCC structure, function and distribution (Catterall, 2005). Calcium currents recorded in different cell types have diverse physiological and pharmacological properties, therefore the above described alphabetical nomenclature was adjusted for the distinct classes of calcium currents. Nowadays, the accepted VDCC nomenclature is as follows: L-type VDCC is the generic name for the subgroup of HVA VDCCs which comprise  $\text{Ca}_v1.1$ ,  $\text{Ca}_v1.2$ ,  $\text{Ca}_v1.3$  and  $\text{Ca}_v1.4$  channels, while the other two subgroups of HVA VDCCs include  $\text{Ca}_v2.2$  (N-type) and  $\text{Ca}_v2.1$  (P/Q-type). The LVA group of VDCCs consists of  $\text{Ca}_v3.1$ ,  $\text{Ca}_v3.2$  and  $\text{Ca}_v3.3$  (T-type) VDCCs, while the IVA group contains the  $\text{Ca}_v2.3$  channel (R-type) (Catterall, 2005). The summary of VDCC types and nomenclature is

given in Tables 3 and 4, together with an overview of their expression sites and cellular functions (Table 3) and type-specific inhibitors (Table 4).

Channel name	Channel type	Localization	Cellular functions
Ca <sub>v</sub> 1.1	L	skeletal muscles; transverse tubules	excitation-contraction coupling
Ca <sub>v</sub> 1.2	L	cardiac myocytes; smooth muscle myocytes; endocrine cells; neuronal cell bodies; proximal dendrites	excitation-contraction coupling; hormone release; regulation of transcription; synaptic integration
Ca <sub>v</sub> 1.3	L	endocrine cells; neuronal cell bodies and dendrites; cardiac atrial myocytes and pacemaker cells; cochlear hair cells	hormone release; regulation of transcription; synaptic regulation; cardiac pacemaking; hearing; neurotransmitter release from sensory cells
Ca <sub>v</sub> 1.4	L	retinal rod and bipolar cells; spinal cord; adrenal gland; mast cells	neurotransmitter release from photoreceptors
Ca <sub>v</sub> 2.1	P/Q	nerve terminals and dendrites; neuroendocrine cells	neurotransmitter release dendritic Ca <sup>2+</sup> transients; hormone release
Ca <sub>v</sub> 2.2	N	nerve terminals and dendrites; neuroendocrine cells	neurotransmitter release dendritic Ca <sup>2+</sup> transients; hormone release
Ca <sub>v</sub> 2.3	R	neuronal cell bodies and dendrites	repetitive firing; dendritic Ca <sup>2+</sup> transients
Ca <sub>v</sub> 3.1	T	neuronal cell bodies and dendrites; cardiac and smooth muscle myocytes	pacemaking; repetitive firing
Ca <sub>v</sub> 3.2	T	neuronal cell bodies and dendrites; cardiac and smooth muscle myocytes	pacemaking; repetitive firing
Ca <sub>v</sub> 3.3	T	neuronal cell bodies and dendrites	pacemaking; repetitive firing

**Table 3: Detailed overview of the localization and cellular functions of different VDCC types.** Blue colour indicates high voltage activated (HVA), yellow intermediate voltage activated (IVA) and violet low voltage activated (LVA) VDCCs. Adapted from Catterall, *Pharmacol Rev*, 2005

Channel type	Channel name	Pore-forming subunit	Pharmacology (type-specific blockers)
L-type	Ca <sub>v</sub> 1.1	α <sub>1S</sub>	TaiCatoxin, Calciseptine, Calcicludine, Dihydropyridines, Benzothiazepine
	Ca <sub>v</sub> 1.2	α <sub>1C</sub>	
	Ca <sub>v</sub> 1.3	α <sub>1D</sub>	
	Ca <sub>v</sub> 1.4	α <sub>1F</sub>	
P/Q-type	Ca <sub>v</sub> 2.1	α <sub>1A</sub>	ω-agatoxin IVA, ω-agatoxin TK, ω-conotoxin MVIIC
N-type	Ca <sub>v</sub> 2.2	α <sub>1B</sub>	ω-conotoxin GVIA, ω-conotoxin MVIIA, ω-conotoxin MVIIC, ω-grammotoxin SIA
R-type	Ca <sub>v</sub> 2.3	α <sub>1E</sub>	SNX-482
T-type	Ca <sub>v</sub> 3.1	α <sub>1G</sub>	Kurtoxin
	Ca <sub>v</sub> 3.2	α <sub>1H</sub>	
	Ca <sub>v</sub> 3.3	α <sub>1I</sub>	

**Table 4: Summary of nomenclature and pharmacology of VDCCs**

Blue colour indicates high voltage activated (HVA), yellow intermediate voltage activated (IVA) and violet low voltage activated (LVA) VDCCs. Adapted from Zamponi G, *Voltage-gated calcium channels*, 2005.

VDCCs have been biochemically characterized as complex proteins composed of four or five distinct subunits that are encoded by multiple genes (Catterall, 2005). The α<sub>1</sub> subunit of 190 to 250 kDa is the largest subunit, and it incorporates the conduction pore, the voltage sensor and gating apparatus, and most of the known sites of channel regulation by second messengers, drugs, and toxins. Like the α subunits of sodium channels, the α<sub>1</sub> subunit of VDCCs is organized in four homologous domains (I–IV), with six transmembrane segments (S1–S6) in each. The S4 segment serves as the voltage sensor. The pore loop between transmembrane segments S5 and S6 in each domain determines ion conductance and selectivity. An intracellular β subunit and a transmembrane, disulfide-linked α<sub>2</sub>δ subunit complex and a γ subunit are components of most types of calcium channels (Fig.2.3. a, b).

Although these auxiliary subunits modulate the properties of the channel complex, the pharmacological and electrophysiological diversity of calcium channels arises primarily from the existence of multiple α<sub>1</sub> subunits (Fig.2.3c).

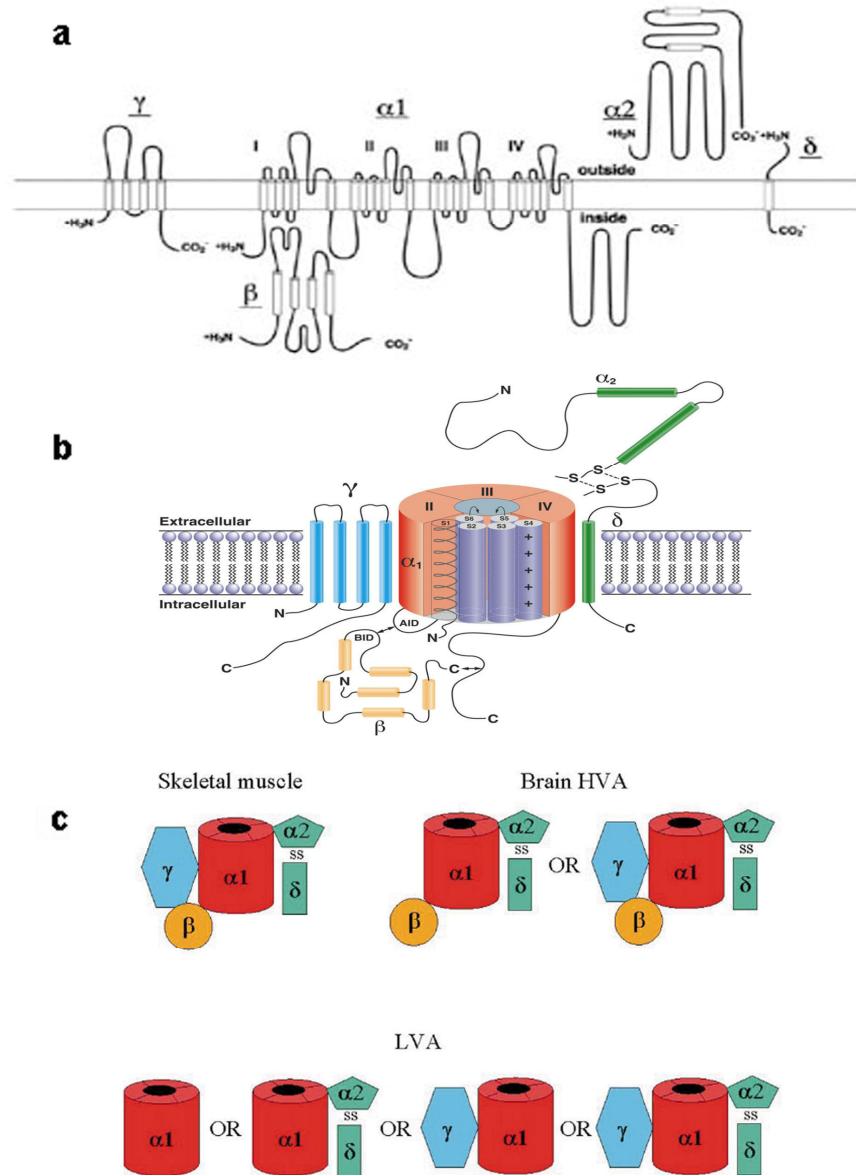


**Fig.2.3: Schematic representations of VDCC structure and possible combinations of different subunits**

(a) The scheme represents the subunit composition and structure of  $Ca_v1$  and  $Ca_v2$  channels. Predicted  $\alpha$  helices are depicted as cylinders. The lengths of lines correspond approximately to the lengths of the polypeptide segments represented. Scheme adapted from Catterall, 2005.

(b) Schematic representation of the heteromeric assembly pattern and topology of the  $\alpha_1\alpha_2\delta\beta\gamma$  complex. 4 homologous repeats of the pore-forming  $\alpha_1$  subunit are shown in red, with a cut-open view of repeat I showing the 6 putative transmembrane  $\alpha$  helices (S1 helix and S2-S6 purple columns). Scheme adapted from Randall, 1999.

(c) The scheme illustrates the most likely subunit combinations exhibited by different VDCC classes. Adapted from Randall, 1999.

Despite of these extensive data on VDCC distribution, the presence of VDCCs in the rat optic nerve is still an ambiguous one. One of the reasons is the fact that ON axons are of too small diameter (0.77  $\mu\text{m}$  is the mean diameter of the rat ON) to allow voltage or patch-clamp studies (Oozeer, 2006). However, it is possible to investigate action potential characteristics by means of extracellular recordings of compound action potentials (CAP) coupled with pharmacological exploration (Lev-Ram and Grinvald, 1986; Fern, 1995; Brown, 2000). Other techniques used to detect VDCC expression in the rat ON include confocal fluorescence imaging of intracellular calcium, usually after selective dye labeling of axons and glial cells which allows for separation of calcium transients to axonal and glial ones (Sun and Chiu, 1999; Stys, 2000), immunological stainings for light, fluorescent, confocal and electron microscopy, as well as formulating simulations of axonal excitability based on the Hodgkin-Huxley model which would enable a prediction of the conditions under which the potential contribution of a  $\text{Ca}^{2+}$  current to the evoked action potential could be measured (Brown, 2003; Oozeer, 2006).

To our knowledge, our work is the first which uses MRI to investigate VDCC distribution.

## **2.7. VDCCs as therapeutic targets**

Given that VDCCs link membrane potential changes of excitable cells to intracellular processes, including regulated secretion of neurotransmitters and hormones, muscle contraction and gene transcription (detailed in Table 3), they are attractive targets for the development of novel pharmacological agents. Therapeutic approaches targeting VDCCs might be useful for a broad variety of diseases originating from excitable tissues, from the central and peripheral nervous systems to the endocrine and cardiovascular apparatus. Currently, blockers of VDCCs are most widely used to treat cardiovascular ailments. These agents act largely via block of just one type of VDCCs, namely L-type. However, in our study, we focused on VDCCs as therapeutic targets for the treatment of neurological diseases.

Several authors showed protective effect of VDCC antagonists in animal models of anoxia or ischemia of the CNS. The synthetic  $\omega$ -conotoxin MVIIA (SNX-111), which selectively blocks depolarization-induced calcium fluxes through neuronal N-type VDCCs, protected pyramidal neurons in the CA1 subfield of the hippocampus from

damage caused by transient forebrain ischemia (Valentino, 1993) and also reduced cortical infarct size in rats subjected to 1h focal cerebral ischemia (Bowersox., 1997). A neuroprotective effect of N-type VDCC blocker was observed in a rat model of spinal ischemia as well (Burns, 1999). Simultaneous block of L-type and N-type VDCCs resulted in postanoxic compound action potential (CAP) recovery in a model of anoxia-induced white matter injury, studied on the isolated rat optic nerve (Fern, 1995) and on dorsal column axons of the rat spinal cord (Imaizumi, 1999).

Taken together, these data suggest that VDCCs are involved in both CNS grey and white matter anoxic and ischemic injury, implicating that strategies directed against  $\text{Ca}^{2+}$  influx via VDCCs may provide protection for a broad spectrum of CNS regions. Furthermore, an altered distribution of VDCCs was detected both in MS and EAE (Kornek, 2001). An amelioration of the disease after application of VDCC blockers has also been demonstrated in a mouse model of EAE. In this study, spinal cord samples showed reduced inflammation and axonal pathology which supports the hypothesis that calcium influx via VDCCs plays a significant role in the development of neurological disability and white matter damage in EAE and MS (Brand-Schieber, 2004).

Some of the most specific VDCC blockers belong to the class of peptide toxins from marine snails (conotoxins) and spiders (agatoxins, grammotoxin). One of the best-characterized species of cone shell marine snails is *Conus geographus*, the venom of which contains, among other toxins, sodium channel blockers ( $\mu$ -conotoxins), acetylcholine receptor blockers ( $\alpha$ -conotoxins), and calcium channel blockers ( $\omega$ -conotoxins) (Olivera, 1987; Norton, 1999).  $\omega$ -conotoxins are a large family of structurally related peptides with a wide range of specificities for different types of VDCCs. The individual peptides in a conotoxin family are typically each selectively targeted to a diverse set of different molecular isoforms within the same ion channel family (Terlau, 2004). Their high selectivity has made them enormously valuable as physiological tools and as a new class of therapeutics for pain management (Malmberg and Yaksh, 1995; Bowersox, 1996) and ischemic brain injury (Valentino, 1993; Fern, 1995). The most frequently used ones are listed in the Table 4.

For example,  $\omega$ -conotoxin MVIIA, entered clinical practice in its synthetic form known as ziconotide or SNX-111 (Prialt ®) for the treatment of chronic neuropathic

pain associated with injury, surgery, cancer and AIDS, especially for those patients who did not respond to intrathecal opioids anymore (Norton, 1999).

## **2.8. Magnetic resonance imaging (MRI) for visualization of MS and EAE pathology**

MRI allows an *in vivo* assessment of several aspects of MS or EAE-related pathological processes, including early inflammation, tissue degradation, and scar formation, and is currently regarded as the gold standard for clinical evaluation of the disease status in MS patients (Rausch, 2003). Furthermore, MRI allows the detection of spatial and temporal dissemination of MS lesions earlier than it is possible by clinical assessments (Zivadinov, 2006). A variety of conventional MRI protocols, in conjunction with clinical assessment, are now routinely used to increase the accuracy of diagnosis and long-term prognosis of multiple sclerosis. For example, multiple regions in which the signal is diminished (“black holes”) in T1-weighted MRI, correspond to chronic lesions in MS (Noseworthy, 2000). The contrast gadolinium-enhanced lesions on T1-weighted images reflect increased blood-brain barrier permeability associated with active inflammatory activity. T2-weighted hyper-intense lesions are related primarily to increased water content and thus cannot distinguish between inflammation, edema, demyelination, Wallerian degeneration, and axonal loss. Changes in the number and volume of lesions on T2-weighted MRI (referred to as the T2-weighted lesion load) are sensitive but non-specific indicators of disease activity and the response to treatment (Noseworthy, 2000). Conventional MRI metrics are not sufficiently sensitive to detect invisible brain damage in the normal appearing brain tissue, and they do not show a reliable correlation with clinical measures of disability. However, numerous studies showed that they can improve accuracy in the diagnosis and prognosis of MS (Zivadinov, 2006). Recently, non-conventional MRI techniques have been introduced to increase the accuracy of diagnosis and prognosis of MS. Several studies have used brain atrophy, T1-hypointense lesion volume, magnetization transfer imaging, diffusion-weighted imaging and magnetic resonance spectroscopy to test whether the extent and severity of tissue loss in lesions and in normal appearing grey and white matter at the time of clinically isolated syndrome may have a diagnostic and prognostic value (Zivadinov, 2006). These MRI techniques

represent a powerful tool to non-invasively study different pathological substrates of lesions and microscopic tissue changes.

Several comparative studies showed significant correlation between MRI findings and histopathology in animal models of MS (Morrissey, 1996; Schellenberg, 2007). Significant decrease in T1 relaxation time during the course of EAE was detected in several EAE models (Seeldrayers, 1993; Boretius 2007, in press).

Contrast-enhanced T1-weighted imaging using extracellular contrast agents allows better visualization of anatomical structures both in healthy and affected animals. Furthermore, combination of different contrast agents may provide broader information on the state of the disease and/or events occurring during the course of EAE. For example, detection of gadolinium-DTPA in the CNS implies BBB disruption (Ding, 2006), while manganese enhancement in definite areas may indicate increased calcium influx (Boretius, 2007, in press). Recently superparamagnetic iron oxide (SPIO) particles as well as ultrasmall superparamagnetic iron oxide (USPIO) nanoparticles (Rausch, 2003) have been introduced as a contrast agent to detect macrophage migration *in vivo* by MRI (Linker, 2006).

## **2.9. Manganese enhanced MRI**

Manganese has long been used as an MRI contrast agent because this paramagnetic ion induces shortening of the spin-lattice relaxation time constant, T1, which yields positive contrast enhancement in T1-weighted MRI, specific to tissues in which the ion has accumulated. Provided that  $Mn^{2+}$  remains compartmentalized after exogenous administration, it can be used for delineating targeted tissue elements, such as the optic nerve (Watanabe, 2001). The manganese ion ( $Mn^{2+}$ ) has been used in biomedical research as an indicator of calcium ( $Ca^{2+}$ ) influx because it is well established that  $Mn^{2+}$  enters cells through voltage-dependent calcium channels (VDCC) (Pautler R, 2006; Koretsky, 2004). However, further pharmacological dissection in order to distinguish the influence of different VDCC types to manganese influx was not performed so far.

## Aim of the study

The aim of our study was to address the following specific questions: 1. Do VDCCs play a pathophysiological role for inflammation-induced neurodegeneration? 2. Which type of VDCCs is involved in increased calcium influx occurring in neuroinflammation? 3. Which cell types express VDCCs involved in increased calcium influx in optic neuritis? 4. Would pharmacological intervention targeted to VDCCs influence the optic neuritis pathology?

In order to answer these questions we have used *in vivo* manganese-enhanced MRI and *in vivo* calcium-imaging coupled with application of VDCC type-specific blockers. For *post-mortem* analysis of VDCC expression in the optic nerve, we have performed immunohistochemistry for the pore-forming subunits of VDCCs. We have used histopathological stainings and immunohistochemistry (IHC) to assess pathology of optic neuritis, namely inflammation, demyelination and axonal degeneration. These were IHC for ED1 (marker of macrophages), Luxol fast blue and Bielschowsky axon impregnation, respectively.

We have also performed double labeling IHC for different cell-type specific markers together with the antibody for the pore-forming subunit of N-type VDCCs, in order to establish which cell types express this type of VDCCs.

Furthermore, we have applied a specific blocker of N-type VDCCs,  $\omega$ -conotoxin GVIA, via the intracerebroventricular continuous infusion, to test if this specific blocker can produce neuroprotective effect in the MOG-induced optic neuritis.

## 3 Methods

### 3.1. Animals

Female Brown Norway rats 8–10 weeks of age were used in all experiments. They were obtained from Charles River (Sulzfeld, Germany) and kept under environmentally controlled conditions without the presence of pathogens. All experiments that involved animal use were performed in compliance with the relevant laws and institutional guidelines. These experiments have been approved by the local authorities of Braunschweig, Germany.

### 3.2. Immunogen

Recombinant rat MOG (rrMOG), corresponding to the N-terminal sequence of rat MOG (amino acids 1–125), was expressed in *Escherichia coli* and purified to homogeneity by chelate chromatography (Weissert, 1998). The purified protein in 6 M urea was then dialysed against 0.01 M sodium acetate, pH 3, to obtain a preparation that was stored at -20° C.

### 3.3. Induction and evaluation of EAE

The rats were anaesthetized by inhalation of diethylether and injected intradermally at the base of the tail with a total volume of 200 µl inoculum, containing 100 µg rrMOG in saline emulsified (1:1) with complete Freund's adjuvant (CFA) (Sigma, St Louis, MO, USA) containing 200 µg heat-inactivated *Mycobacterium tuberculosis* (strain H 37 RA; Difco Laboratories, Detroit, MI, USA). Rats were scored for clinical signs of EAE and weighed daily. The signs were scored as follows: grade 0.5, distal paresis of the tail; grade 1, complete tail paralysis; grade 1.5, paresis of the tail and mild hind leg paresis; grade 2.0, unilateral severe hind leg paresis; grade 2.5, bilateral severe hind limb paresis; grade 3.0, complete bilateral hind limb paralysis; grade 3.5, complete bilateral hind limb paralysis and paresis of one front limb; grade 4, complete paralysis (tetraplegia), moribund state, or death. Cumulative score was calculated as the sum of daily clinical scores.

### **3.4. Retrograde labeling of RGCs**

Two weeks before immunization, adult Brown Norway rats were anaesthetized with intraperitoneal injection of ketamine 10% (0.65 ml/kg; Inresa, Germany) together with xylazine 2% (0.35 ml/kg; Albrecht, Aulendorf, Germany) and placed in a stereotactic frame. The skin was incised mediosagittally, and holes were drilled into the skull above each superior colliculus (6.8 mm dorsal and 2 mm lateral from bregma). We injected stereotactically 2  $\mu$ l of the fluorescent dye fluorogold (FG; 5% in normal saline) (Fluorochrome Inc., Englewood, CO, USA) into both superior colliculi. For postoperative analgesia, carprofen (5 mg/kg in saline, Rimadyl®, Pfizer, Germany) was given subcutaneously.

### **3.5. Quantification of RGC density**

At the end of the MRI recordings or at the end of the treatment study, the rats were humanely sacrificed with CO<sub>2</sub> and were perfused via the aorta with 4% paraformaldehyde (PFA) in phosphate-buffered saline (PBS). The brain, the ONs and both eyes were removed, and the retinas were dissected and flat-mounted on glass slides. They were examined by fluorescence microscopy (Axiophot 2; Zeiss, Göttingen, Germany) using an UV filter (365/397 nm). RGC densities were determined by counting of labelled cells in three areas (62 500  $\mu$ m<sup>2</sup>) per retinal quadrant at eccentricities of 1/6, 3/6, and 5/6 of the retinal radius. Cell counts were performed by two independent investigators following a blind protocol.

### **3.6. Optic nerve histopathology**

At the end of the MRI recordings or at the end of the treatment study, the animals were perfused with 4% PFA in PBS and postfixed overnight in 4% PFA. ONs were removed and embedded in paraffin. Histological evaluation was performed on 0.5  $\mu$ m thick slices stained with Luxol-fast blue and Bielschowsky's silver impregnation to assess demyelination and axonal pathology, respectively. Demyelinated areas were determined as a percentage of the whole ON cross-section. The surface area of the ON was measured using the AxioVision 4.5 software (Carl Zeiss, Germany). Axonal densities were determined in cross sections of the ONs stained by Bielschowsky's

silver impregnation. Overview photographs (200x magnification) and high-magnification photographs (1000x magnification) were made with a CCD camera (Color View II; Soft imaging System1) and Axioplan 2 microscope (Carl Zeiss, Germany). The number of axons in each ON was counted using a custom-made eyepiece with a grid (Carl Zeiss, Germany) which allowed for a stereological counting. Three grid areas were randomly positioned within the area of the ON cross-section. The average of three counts was expressed as percentage of the mean number of axons in the ONs of a healthy control group of BN rats (n=8; 16 ONs). Due to substantial changes during optic neuritis, it was not possible to blind the observer as to whether a section was from a MOG-immunized animal or a healthy control. However, the investigator who performed neuropathological examinations was blinded to the MRI data as well as to the results of the treatment study with  $\omega$ -conotoxin GVIA.

### 3.7. Immunohistochemistry

Immunohistochemistry was performed in serial sections of paraffin-embedded ONs and spinal cords. The following standard protocol was followed:

- The paraffin sections were deparaffinized and
- rehydrated by placing in 2 changes of xylol (10 min each)
- followed by 6 changes, 2 min each, in ethanol (EtOH) of descending concentrations (2 x 100%-2 x 90%-70%-50%),
- followed by cold running tap water
- microwave antigen retrieval was performed by heating the slides in 0.2% citrate buffer pH=6.0 for 10 min at 800W
- cooling down (15 min) and washing in PBS for 2 x 5 min
- quenching of endogenous peroxidase by immersing the slides in 3% H<sub>2</sub>O<sub>2</sub>/PBS for 10 min at room temperature (RT)
- wash with PBS (2 x 5 min)
- blocking for 1h at RT with 10 % serum (a) or in 10 % serum in 0.3 % Triton X-100 (b)
- applying primary antibody in appropriate dilution (c)
- Incubation overnight at 4°C

- At this point staining may proceed with various secondary antibodies:
- for light microscopy
  - incubation with secondary antibody (d) 1h/RT
  - sections were incubated with VECTASTAIN® Elite Universal ABC kit (Vector, Burlingham, USA) 1h/RT
  - Color development was achieved by incubating the sections for 3 min/RT
  - in DAB substrate kit for peroxidase (Vector, Burlingham, USA)
  - stopping the reaction with distilled water (5 min/RT)
  - followed by 10 min in Haemalaun and HCl-EtOH for counterstaining
  - after dehydration through the ascending series of EtOH and
  - delipidation in xylol (2 x 10 min)
  - the slides were coverslipped using Roti® - Histokitt II (Carl Roth, Germany ) mounting solution
- for fluorescence microscopy
  - application of secondary antibodies (e) 1h/RT in dark
  - wash in PBS (3 x 5 min)
  - 5 min immerse in DAPI (Sigma-Aldrich, Germany)
  - the slides were coverslipped using Shandon Immu-Mount (Thermo Electron Corporation, UK) mounting solution

a) For light microscopy IHC for anti- $\beta$ -APP and anti-ED1, the blocking was performed using a 10 % horse serum (Sigma-Aldrich, Germany)

b) For anti-N-type calcium channel IHC light microscopy, blocking was done with 10 % normal donkey serum (Sigma-Aldrich, Germany) in 0.3 % Triton X-100 (Sigma-Aldrich, Germany) and for fluorescence microscopy with 10 % normal goat serum (Sigma-Aldrich, Germany) in 0.3 % Triton X-100

c) The following primary antibodies were used:

- rabbit anti-N-type calcium channel (anti- $\alpha_{1B}$ ) (Sigma-Aldrich, Germany; dilution 1:1000),
- mouse anti- $\beta$ -APP (Chemicon, USA; 1:1000),
- mouse anti-ED1 (CD68, Serotec, UK; 1:500),
- mouse anti-glial fibrillary acid protein (GFAP, Dianova, Germany, 1:100)

- mouse anti-myelin 2', 3'-cyclic nucleotide 3'-phosphodiesterase (myelin CNPase) (SMI 91, Covance, USA; 1:200).

d) Secondary antibodies for light microscopy IHC:

- biotinylated donkey anti-rabbit (Chemicon USA, 1:400)
- biotinylated goat anti-rabbit IgG (Vector, Burlingham, USA; 1:200),
- biotinylated goat anti-mouse IgG (Vector, Burlingham, USA; 1:200),
- biotinylated horse anti-mouse IgG (Vector, Burlingham, USA; 1:200),

e) Secondary antibodies for fluorescence microscopy IHC:

- Cy3-labelled goat anti-rabbit IgG (Jackson Immunoresearch, USA; 1:600),
- Alexa 488-labelled goat anti-mouse IgG (Molecular Probes, Netherlands, 1:400).

Control sections were incubated in the absence of primary antibodies. As positive controls, spinal cord sections, where the expression pattern for VDCCs is well described (Kornek, 2001), were always stained in parallel with ON sections to assure the efficacy of each staining trial. Stereological quantitative analysis of ED1 and  $\alpha_{1B}$ -labelled serial sections was performed using a calibrated eyepiece. The immunopositive sites were counted in 3 randomly selected areas per ON. The counts were performed independently by two investigators following a blind protocol.

### 3.8. Experimental setup for *in vivo* manganese enhanced MRI

30 animals underwent MRI at day 14 post immunization when the average integrity of the blood-brain barrier is maximally reduced and allows VDCC blockers to penetrate into the CNS. Anaesthesia was induced by medetomidine (0.25 mg/kg, s.c., Domitor®, Pfizer, Germany) and ketamine (25 mg/kg, i.v., Medistar, Germany). The animal numbers decreased at later time points due to advanced neurological impairment. After muscular relaxation, the animals were intubated under visual control with a purpose-built endotracheal tube (1.4 mm inner diameter, 2.1 mm outer diameter), and artificially ventilated. Anaesthesia was maintained using isoflurane (0.25 – 0.5% in oxygen and ambient air (1:1.5)). The anaesthetized and intubated animals were placed in the magnet in a supine position with the head firmly fixed by a home-build stereotaxic device. For the application of contrast agents, the rats were provided with a permanent venous catheter in one of the tail veins.

All MRI measurements were performed at 2.35 T using a MRBR 4.7/400 mm magnet (Magnex Scientific, Abington, UK) equipped with a DBX system (Bruker Biospin, Ettlingen, Germany). A birdcage radio frequency coil (154 mm inner diameter) was used for excitation together with a saddle-shaped surface coil for signal reception (both from Bruker Biospin, Ettlingen, Germany). High-resolution T1-weighted data sets with an isotropic resolution of 230  $\mu\text{m}$  were acquired using 3D FLASH (TR/TE = 17.0 ms/4.36 ms, flip angle = 25 degree). The relatively short TE was chosen to ensure opposite-phase conditions for fat and water. After acquisition of pre-contrast T1-weighted images, the animals received  $\text{MnCl}_2$  (0.05 mmol/kg, Sigma-Aldrich, USA) via the vein catheter.  $\text{Mn}^{2+}$ -enhanced T1-weighted MRI was performed 10 minutes as well as 24 h and 48 h after  $\text{MnCl}_2$  administration. Some animals additionally received a VDCC blocker or AMPA/kainate receptor antagonist which was administered shortly before  $\text{MnCl}_2$  injection. The following VDCC antagonists were applied: diltiazem (20 mg/kg i.p.; Sigma-Aldrich, Germany),  $\omega$ -conotoxin GVIA (10  $\mu\text{g}/\text{kg}$  i.v.; Anaspec, USA), amlodipine (5 mg/kg p.o.; LKT Laboratories, USA), amiloride (100  $\mu\text{mol}/\text{kg}$  i.v.; Sigma-Aldrich, Germany), or  $\omega$ -agatoxin IVA (20  $\mu\text{g}/\text{kg}$  i.v.; Alomone, Israel). NBQX (30 mg/kg i.p.; Tocris Bioscience, USA) was used for AMPA/kainate receptor blockade. Drug concentrations were chosen according to previously described dosages sufficient to achieve a selective channel blockade in rat models of EAE (Smith, 2000), neurogenic pain and vasodilatation (Akerman, 2003), or patch clamp studies on isolated nerves (Furukawa, 1997; Sun, 1999).

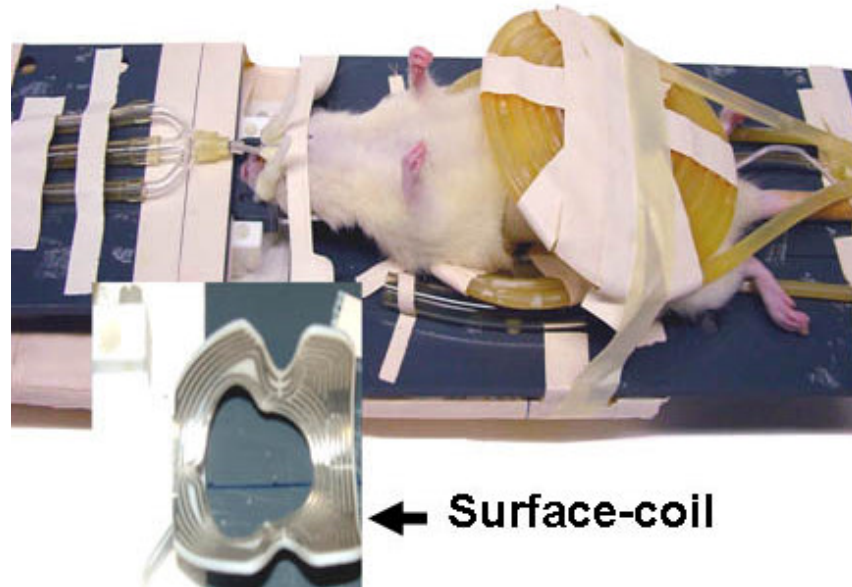


**Fig.3.1: Position of the animal in the holder used for placing in the MR scanner.**

Magnified image shows saddle-shaped surface coil. The image represents only the position of the animal in the holder (The photo shows Wistar rat, we used BN). Image courtesy of Dr. Susann Boretius, NMR in Biomedicine GmbH, Max-Planck Institute for Biophysical Chemistry, Göttingen, Germany

### 3.9. Analysis of MR images

For quantitative image analyses, MRI sections parallel to the optic nerve were used to determine a suitable region-of-interest (ROI). Quantitative ROI analyses were based on MRI signal intensities (SI) in the optic nerve normalized to the intensity of nearby grey matter using Paravision 3.2 (Bruker Biospin, Ettlingen, Germany) (Fig. 3.2). The ratio of the normalized signal intensities after and before application of  $Mn^{2+}$  was calculated to determine the efficiency of the applied antagonists to block respective  $Ca^{2+}$  channels.

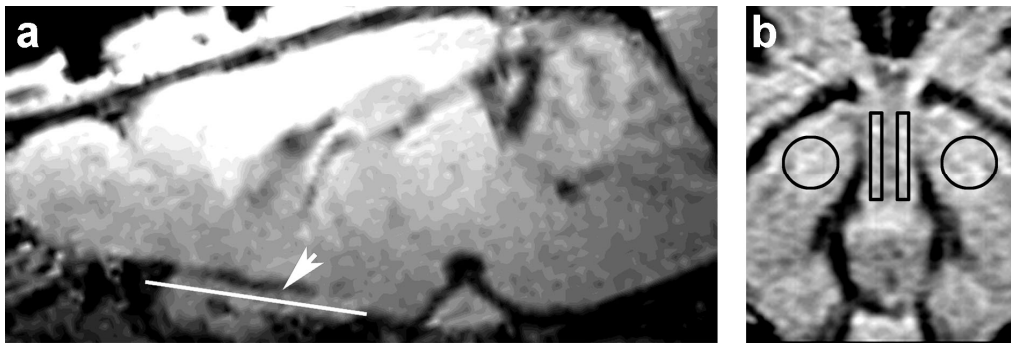


**Fig.3.2: Selected regions of interest (ROIs) used for analysis of MR images**

- (a) Mid-sagittal section of a T1-weighted MRI data set from a control animal. The horizontal line parallel to the optic nerve demonstrates the section orientation shown in b)
- (b) In each optic nerve (ON), there are identical square ROIs. Two circular ROIs are positioned in the brain tissue surrounding the optic nerve. SI measured in selected ROIs was used to calculate ratio of normalized SI before and after  $Mn^{2+}$  application (detailed description is given in the text).

### 3.10. Labeling of the optic nerves with a $Ca^{2+}$ sensitive dye

17 rats underwent the procedure for *in vivo*  $Ca^{2+}$  imaging. Animals were anesthetized by intraperitoneal injection of chloralhydrate (420 mg/kg bodyweight). Using a Hamilton syringe, 3  $\mu$ l of Oregon Green 488 BAPTA-1 AM ester (OGB) were injected into the vitreous body. OGB is then taken-up by RGCs and transported anterogradely in the axons forming the ON. Uptake of OGB in the ON reached a plateau after ~2h and the ON was then prepared for *in vivo*  $Ca^{2+}$  imaging. After performing a mediosagittal skin incision to the skull, the orbita was opened by dissecting the soft tissue parallel to the orbital rim. The intraorbital glands were subtotaly resected. After spreading of the superior extraocular muscles, the ON was exposed by longitudinal incision of the nerve sheath. A tie of fine surgical thread (10/0, Ethilon) was placed loosely around the ON to highlight the region of interest.

### 3.11. *In vivo* calcium-imaging

The anesthetized rat was placed on a platform below the objective ("Achromplan" 40x/0.8 W Ph2, Zeiss, Göttingen) and the objective was lowered on to the exposed dye-loaded ON. The space between the objective and ON was filled with calcium-free

isotonic 0.9% NaCl solution. OGB was excited at 488 nm and collected through a 522 nm bandpass filter using fluorescence microscope (Axioplan-2, Zeiss, Göttingen, Germany). In order to quantify the extent of photobleaching, 50 images (1/s) were taken before inducing depolarization. To induce depolarization 10  $\mu$ l of a KCl solution (160 mM) were injected intravitreally.  $\omega$ -conotoxin GVIA (Möbitec, Germany) was applied topically to the exposed nerve, for 30 minutes before inducing depolarization, in a dose of 3  $\mu$ g per ON according to previous experiments described by Xiao et al (Xiao, 1995).

Data analysis was conducted using ImageJ 1.36b (<http://rsb.info.nih.gov/nih-image/default.html>), based on the mean fluorescence intensity (analysis of mean grey value of each picture).

### **3.12. Intracerebroventricular infusion**

16 rats were implanted with mini-osmotic pumps (model 2004, delivery rate 0.25  $\mu$ l/h, Alzet, USA) and the respective brain infusion kits (model 1, Alzet, USA).  $\omega$ -conotoxin GVIA (6  $\mu$ M) was diluted in sterile artificial cerebrospinal fluid (aCSF) (Harvard Apparatus, USA) immediately before filling of the osmotic pumps. The vehicle-treated control groups of rats received pumps containing aCSF without addition of the blocker. The pumps with the attached brain infusion catheters were primed for 40 h at 37°C in sterile 0.9 % saline according to the instructions from the manufacturer. After that, the pumps were implanted subcutaneously in the interscapular region. The tip of the infusion kit was placed into the right lateral ventricle according to the following stereotactical coordinates: 0.9 mm caudal and 1.4 mm lateral to bregma, 3.6 mm below the dura mater (Paxinos and Watson, 1998). After placement, all incisions were closed with Autoclips (Stoelting, USA). The minipumps yielded a constant infusion rate of 0.25  $\mu$ l/h for a time period of 23 days in the pre-treatment groups and for a time period of 8 days in the “late” treatment groups. During these experiments,  $\omega$ -conotoxin GVIA was delivered at a concentration of 1.5 pmol/h. This protocol was chosen due to results obtained from a preliminary dose-finding trial (data not shown) and according to published data describing chronic intracerebroventricular applications of conopeptides (Malmberg and Yaksh, 1995). After explantation of the pumps, the residual volume was

recovered from the pump reservoir and measured in order to verify the accuracy of the pump delivery. The values were within the range predicted by the manufacturer.

### **3.13. Statistical analysis**

The degree of  $Mn^{2+}$  - induced enhancement within the ONs after application of various VDCC antagonists was compared by Kruskal-Wallis non-parametric ANOVA followed by Dunn's post hoc procedure. These tests were also used for comparing the fluorescence intensities after calcium imaging of healthy and inflamed ONs treated with VDCC blockers. Statistical significances of the histopathological data, differences between RGC densities and the neurological scores were assessed using the non-parametric Mann-Whitney two-tailed test. The Spearman two-tailed test was used to examine the correlation between  $\alpha_{1B}$  expression and percentage of demyelination or axonal survival. The following levels of significance were defined:  $p < 0.05$  to be significant,  $p < 0.01$  to be very significant and  $p < 0.001$  to be highly significant. All statistical analyses were performed using GraphPad Prism software, version 4.00 for Windows (GraphPad Software, San Diego, California, USA).

## 4 Results

### 4.1. In optic neuritis signal intensity in T1-weighted MR images is reduced and $Mn^{2+}$ - induced enhancement is prominent

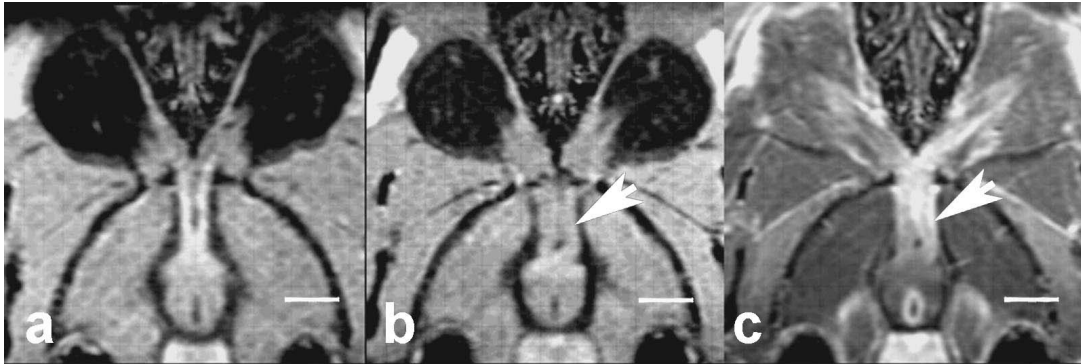


**Fig.4.1: T1-weighted MR images of optic nerves**

(a) ONs from a healthy rat (b) ONs from a rat with MOG-induced optic neuritis, before and (c) after application of manganese ( $Mn^{2+}$ ) as a contrast agent. T1-weighted signal intensity (SI) in inflamed is significantly decreased when compared to healthy ONs. Note the increase in ON diameter in (b) and (c) due to oedema formation. The arrowhead points out to the change in contrast between the optic nerves and the surrounding brain tissue before and after  $Mn^{2+}$ - application. Scale bar = 2 mm.

Sham-immunized controls and rats with optic neuritis underwent T1-weighted 3D MRI before and 10 min after  $Mn^{2+}$  application (Fig. 4.1a–c). Compared to controls inflamed ONs exhibited a marked reduction of the normalized signal intensity (SI) on the pre-contrast T1-weighted images (Fig. 4.1a, b). The SI of the ONs were  $1.09 \pm 0.01$  (n=8) and  $0.94 \pm 0.05$  (n=6) ( $p = 0.029$ ; mean  $\pm$  SEM) for healthy and inflamed ONs, respectively. During optic neuritis, a strong  $Mn^{2+}$  - induced enhancement was evident in the central parts of the ON (Fig. 4.1c), suggestive of an influx of  $Mn^{2+}$  into the cytoplasm of the nerve fibers. Note an increased diameter of ONs with neuritis.

## 4.2. High voltage-activated calcium channels mediate $Mn^{2+}$ - induced enhancement

Because  $Ca^{2+}$  and  $Mn^{2+}$  are of a similar size and of the same positive charge, we investigated whether the routes of entry for these two bivalent cations are the same. Therefore, a previously described MRI protocol (Boretius, 2007 in press) was modified to include the application of pharmacological antagonists of AMPA/kainate receptors and of VDCCs. These were applied immediately prior to  $Mn^{2+}$  during the MR imaging session, allowing the effects of the inhibitors on  $Mn^{2+}$  influx to be detected by the enhanced contrast in T1-weighted MR images.

Initially, the effects of an AMPA/kainate receptor antagonist, NBQX (30 mg/kg i.p) (Smith, 2000), a broad-range blocker of high voltage-activated (HVA) VDCCs, amlodipine (5 mg/kg, p.o) (Furukawa, 1997), and a low voltage-activated VDCC antagonist, specific for T-type VDCCs, amiloride (100  $\mu$ mol/kg i.v) (Turner, 2004 and personal communication) were investigated. Drug concentrations were chosen according to previously described dosages sufficient to achieve a selective channel blockade in rat models of ischemia (Smith, 2000), neurogenic pain and vasodilatation (Akerman, 2003), as well as patch clamp studies on isolated nerves (Sun, 1999). In each trial, the blocker was applied after performing the first T1-weighted FLASH scan and before  $Mn^{2+}$  application.

Application of NBQX (AMPA-block) or amiloride (T-block), alone or in combination, did not have any detectable effect on  $Mn^{2+}$  - induced enhancement (Fig. 4.2b, c). However, application of amlodipine (L+N block), a broad-range blocker of HVA VDCCs, led to a prominent decrease of  $Mn^{2+}$  - induced enhancement (Fig. 4.2d). The normalized SI was measured before and 10 min after application of  $Mn^{2+}$  and used to quantify the effect of the applied antagonists. Mean values  $\pm$  SEM (Fig. 2e) were  $2.62 \pm 0.14$  in controls (n=4),  $2.43 \pm 0.06$  in animals receiving the T blocker (n=3),  $1.85 \pm 0.04$  for T+AMPA blocker (n=3), and only  $1.40 \pm 0.04$  for L+N blocker (n=3).

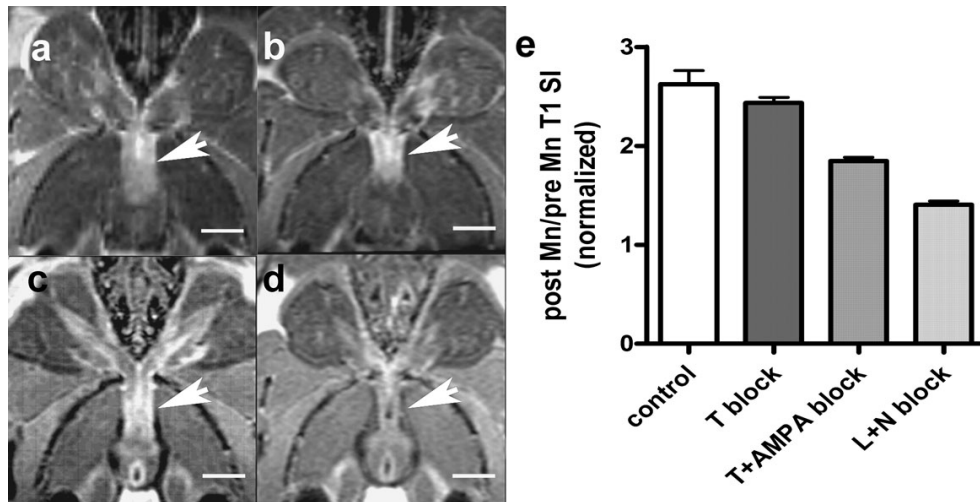


**Fig.4.2: T1-weighted MR images obtained 10 min after Mn<sup>2+</sup> application demonstrating the effects of type-specific VDCC blockers and an AMPA-receptor inhibitor on the Mn<sup>2+</sup>- induced enhancement within the inflamed ONs.**

(a) ON without blocker. (b) A T-type specific VDCC blocker did not reduce Mn<sup>2+</sup> - induced enhancement. (c) The combination of a T-type VDCC blocker and an AMPA-receptor did not reduce Mn<sup>2+</sup> - induced enhancement. (d) Inhibition of L- and N- type VDCCs led to a clear reduction of Mn<sup>2+</sup>- induced enhancement. (e) Normalized signal intensities of the ONs without blocker (*control*), with amiloride (*T block*), with amiloride and NBQX (*T+AMPA block*), and with amlodipine (*L+N block*). Note a trend towards a reduced signal intensity in the animal group which received L- and N- type VDCCs. Error bars represent SEMs..

### 4.3. Mn<sup>2+</sup> enters the inflamed ON via N-type VDCCs

After the most significant inhibition of Mn<sup>2+</sup> uptake was observed using the HVA VDCC blocker, further experiments were performed with higher animal numbers, allowing for full statistical analyses. Our objective was to further dissect the HVA VDCCs involved in Mn<sup>2+</sup> influx, namely L-type, P/Q-type, and N-type VDCCs through the use of more specific antagonists. These included diltiazem, an inhibitor of L-type VDCCs (20 mg/kg i.p) (Sun, 1999),  $\omega$ -conotoxin GVIA (10  $\mu$ g/kg i.v) (Akerman, 2003), a specific blocker for N-type VDCCs, and  $\omega$ -agatoxin IVA (20  $\mu$ g/kg i.v) (Akerman, 2003), a specific inhibitor of P/Q -type VDCCs. The antagonists were applied only to those animals which showed abnormalities in T1-weighted MR images such as increased ON diameter and decreased signal intensity, indicative of

severe optic neuritis (data not shown). In some cases, additional corroboration of optic neuritis was obtained by application of a conventional MRI contrast agent, gadolinium-diethylenetriaminepentaacetic acid (Gd-DTPA), which is widely used to assess a disruption of the BBB (Ding, 2006) (Fig.4.2c,d). Furthermore, following histopathology, only ONs with more than 50 % demyelination were included in the statistical evaluation. Figure 4.3a–d show T1-weighted images of inflamed ONs 10 min after  $Mn^{2+}$  application where ONs of untreated animals are shown in Fig. 3a, and of animals which additionally received the L-type (Fig. 4.3b), the P/Q-type (Fig. 4.3c), and the N-type blocker (Fig. 4.3d). Whereas the normalized SI in animals receiving the L-type ( $1.70 \pm 0.20$ ;  $n=8$ ) or P/Q-type blocker ( $1.82 \pm 0.09$ ;  $n=9$ ) did not significantly differ from controls ( $2.03 \pm 0.13$ ;  $n=14$ ),  $Mn^{2+}$ - induced signal enhancement in the central parts of the ONs was significantly reduced after application of the N-type blocker ( $1.49 \pm 0.04$ ;  $n=7$ ;  $p = 0.038$ , Fig. 4.3g).

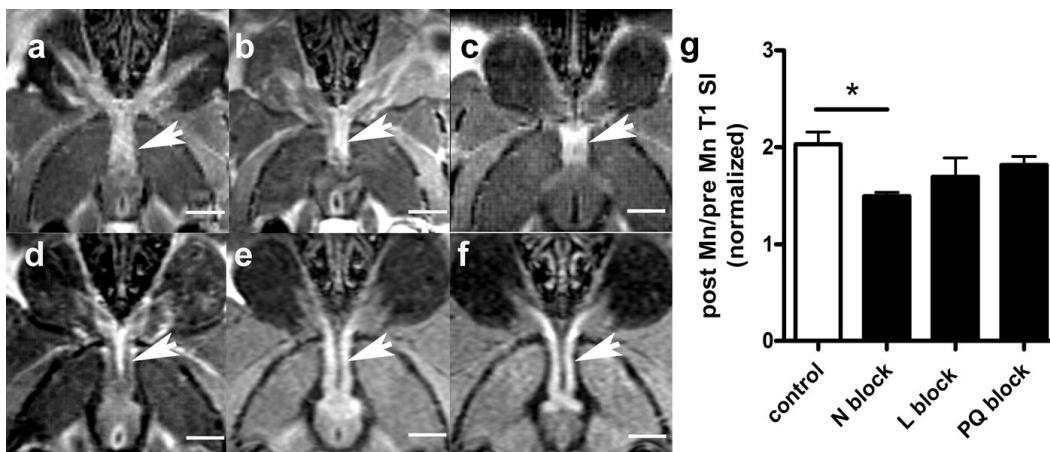


**Fig.4.3: T1-weighted MR images obtained after  $Mn^{2+}$  application demonstrating the effects of type-specific HVA VDCC blockers on  $Mn^{2+}$ -induced enhancement within the inflamed ONs.**

Images (a–d) were taken 10 min after application of  $Mn^{2+}$  without a blocker (a), with the L-type VDCC blocker (b), with the P/Q-type VDCC blocker (c), and with the N-type VDCC blocker (d). Note that application of the N-type VDCC blocker suppresses  $Mn^{2+}$ -induced enhancement within the ONs. However, after degradation of the N-type VDCC blocker (i.e., after 24 h)  $Mn^{2+}$ -induced enhancement of the inflamed ONs recovers (e) and retains up to 48 h (f). (g) Normalized signal intensities of the ONs without blocker (*control*), with  $\omega$ -CTX (*N block*), with diltiazem (*L block*), and with  $\omega$ -agatoxin IVA (*PQ block*). Error bars represent SEMs (\*  $p < 0.05$ ). Scale bar = 2 mm.

In this context, it is important to emphasize that the half-life of the used N-type blocker is  $4.61 \pm 0.59$  h (Bowersox, 1997). In order to look for an enhancement induced by  $Mn^{2+}$  after degradation of  $\omega$ -conotoxin GVIA in the same animals and thereby assure the specificity of the effect, we performed two additional measurements at later time points, 24 h and 48 h after the initial application. MRI performed at 24 h and 48 h after initial application exhibited  $Mn^{2+}$ - induced signal enhancement even in ONs of animals presented with suppressed  $Mn^{2+}$ - induced enhancement 10 min after injection of the N-type blocker. Quantitative analyses revealed a prominent increase in the normalized SI ratio of the ON, both at 24 h ( $1.35 \pm 0.04$ ; n=5) and 48 h after  $Mn^{2+}$  application ( $1.14 \pm 0.09$ ; n=5) (Fig. 3e, f), which was not significantly different from the untreated animals ( $1.42 \pm 0.11$  at 24 h, n=5;  $1.41 \pm 0.12$  at 48 h; n=3).

Furthermore, after 48 hours we observed a spreading of the enhancement along the ON. This spreading progressed up to a certain level and then started decreasing, which is probably due to a combination of axonal transport of  $Mn^{2+}$  and on-going  $Mn^{2+}$  wash-out. These observations are in consistency with previous findings concerning the axonal transport of  $Mn^{2+}$  ions (Watanabe, 2001; Pautler, 1998).

#### **4.4. N-type VDCC expression is up-regulated in optic neuritis and correlates with demyelination pattern**

Because blockade of N-type VDCCs reduced  $Mn^{2+}$  uptake into the inflamed ON, N-type VDCC expression was investigated in more detail. Immunohistochemistry for  $\alpha_{1B}$ , the pore-forming subunit of N-type VDCCs, at the light microscopic level, revealed a significant difference in both the degree and the pattern of N-type VDCC expression between healthy and inflamed ONs. In healthy, myelinated ONs, a modest degree of  $\alpha_{1B}$  immunoreactivity was detected, and quantified as the number of  $\alpha_{1B}$ -positive sites per ON ( $30.8 \pm 0.9$ ; n=8) (Fig.4.4b, h). However, a highly significant up-regulation of expression was seen in MOG-immunized ONs ( $82.7 \pm 5.0$ ; n=10) compared to the ONs of healthy, sham-immunized rats ( $p < 0.0001$ ) (Fig.4.4 d, f and Fig.4.5a). Furthermore, a highly significant positive correlation between the number of  $\alpha_{1B}$ -positive sites per ON and the percentage of demyelination was detected by myelin-specific histopathological staining ( $r = 0.81$ ,  $p < 0.0001$ ; n = 30) (Fig.4.5b). A

highly significant negative correlation was observed between the number of  $\alpha_{1B}$ -positive sites per ON and the percentage of axonal survival ( $r = -0.66$ ,  $p = 0.0002$ ;  $n = 26$ ) (Fig.4.5c) counted after Bielschowsky silver impregnation of axons. In parallel with the  $\alpha_{1B}$  staining of serial ON sections, we stained spinal cord sections from healthy rats which served as positive controls (Fig.4.4g) and showed previously described staining pattern of pronounced staining in regions of high synaptic density (Kornek, 2001).

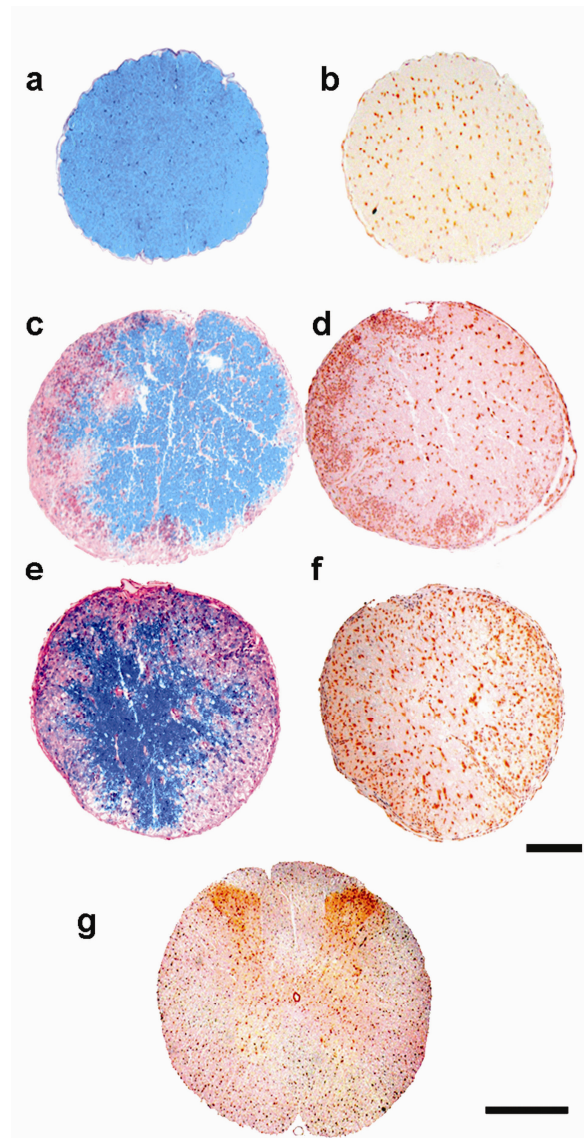
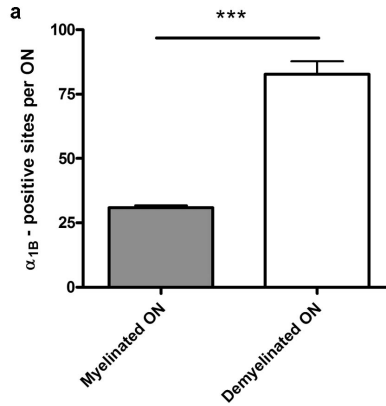
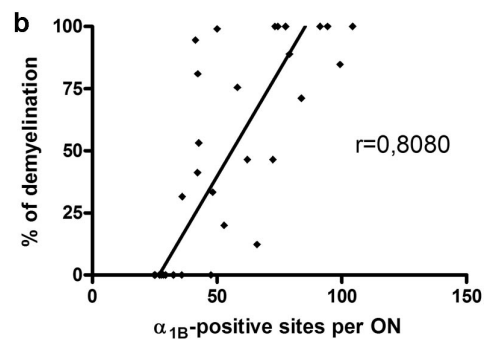


**Fig.4.4: Expression of N-type VDCCs in rat optic nerves during optic neuritis, compared to myelin-specific histopathological staining (LFB)**

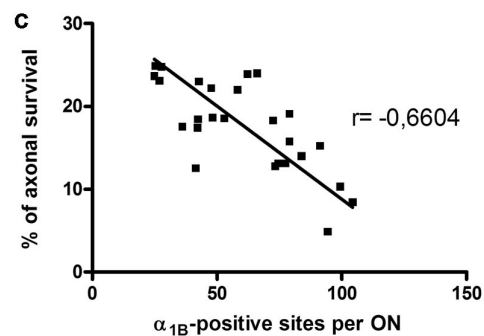
(a) LFB staining of a healthy optic nerve, showing complete myelination (blue area). (b) Same optic nerve as shown in (a) stained for  $\alpha_{1B}$ , the pore-forming subunit of N-type VDCCs. (c) and (e) LFB stainings of optic nerves from rats with MOG-induced optic neuritis. The two representative examples show different degrees and patterns of demyelination (purple areas). (d) and (f) Adjacent serial sections of the optic nerves shown in (c) and (e) stained for  $\alpha_{1B}$ . Note the up-regulation of  $\alpha_{1B}$  in the demyelinated areas. (g) Cross-section of the healthy rat spinal cord, showing intense  $\alpha_{1B}$ - immunoreactivity in regions of high synaptic density. Spinal cord sections were used as positive controls to assure the efficacy of the  $\alpha_{1B}$ -staining. Scale bars = 100  $\mu\text{m}$



(a) Quantification of  $\alpha_{1B}$ -positive sites per optic nerve in myelinated and demyelinated regions, \*\*\*, ( $p < 0.0001$ ;  $n = 10$ ).



(b) Correlation between the numbers of  $\alpha_{1B}$ -positive sites per optic nerve and the percentage of demyelination ( $r = 0.81$ ,  $p < 0.001$ ;  $n = 30$ ).



(c) Correlation between the numbers of  $\alpha_{1B}$ -positive sites per optic nerve and the percentage of axonal survival ( $r = -0.66$ ,  $p = 0.0002$ ;  $n = 26$ ).

**Fig.4.5: Quantitative analysis of  $\alpha_{1B}$  immunoreactivity and comparison to axonal survival and demyelination**

#### 4.5. N-type VDCC expression correlates with immunoreactivity for $\beta$ -amyloid precursor protein

A previous study performed in rat EAE revealed a comparable staining pattern for  $\alpha_{1B}$  and  $\beta$ -amyloid precursor protein ( $\beta$ -APP), an early marker of disturbed axonal transport, in brain and spinal cord tissue of the animals (Kornek, 2001). We investigated the relationship between  $\alpha_{1B}$  and  $\beta$ -APP expression during optic neuritis. Fluorescence microscopy revealed a co-localization of  $\alpha_{1B}$  and  $\beta$ -APP, as shown in Figure 4.6. These results indicate that N-type VDCCs are expressed on degenerating ON axon fibers. However, some immunoreactivity was also detected on astrocytes (Fig. 4.7), as has been previously reported by Kornek and colleagues (Kornek, 2001).

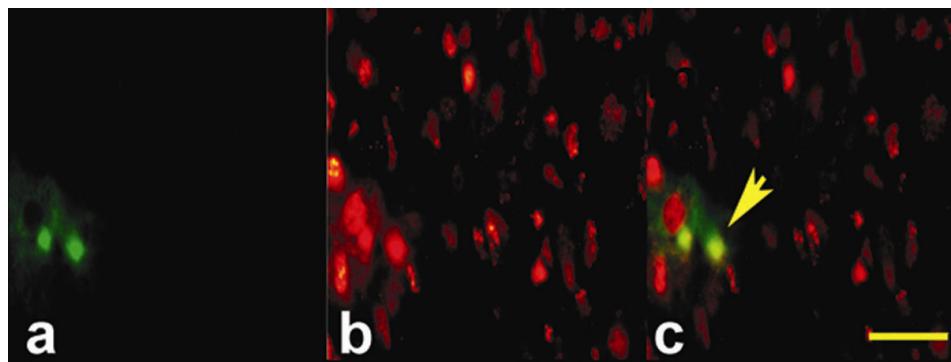


**Fig.4.6: Fluorescent microscopy co-labeling for axonal marker ( $\beta$ -APP) and N-type VDCC ( $\alpha_{1B}$ )**

(a) Immunoreactivity for  $\beta$ -APP and (b)  $\alpha_{1B}$  (c) merged fluorescence microscopy image. The arrow points out to the area of overlaying immunoreactivity. Scale bar = 20  $\mu$ m

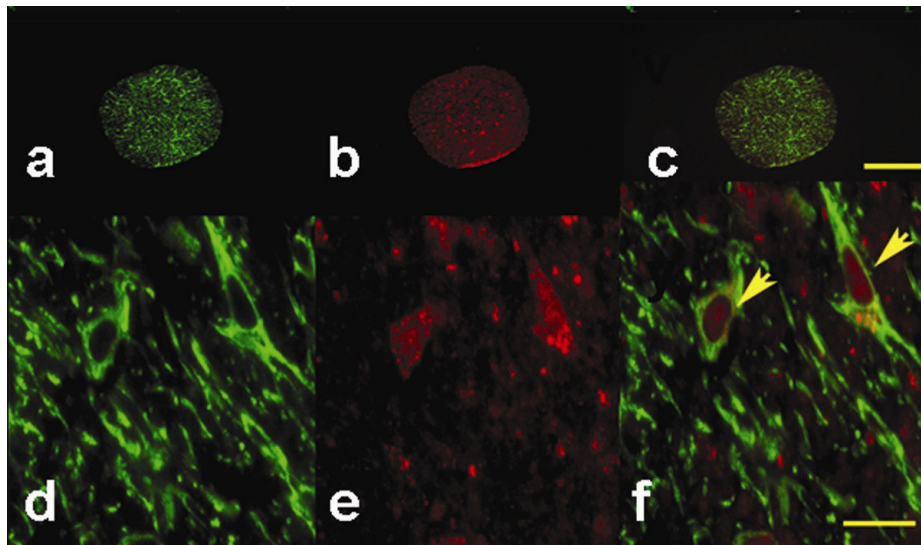


**Fig.4.7: Fluorescent microscopy co-labeling for astrocytic marker (GFAP) and N-type VDCCs ( $\alpha_{1B}$ )**

(a, d) GFAP immunoreactivity (b, e)  $\alpha_{1B}$  immunoreactivity (c, f) merged fluorescence microscopy image. The arrow points out to the area of overlaying immunoreactivity. (a-c) scale bar = 100  $\mu\text{m}$ , (d-f) scale bar = 20  $\mu\text{m}$

#### **4.6. Expression of N-type VDCCs in optic neuritis does not correlate with CNPase reactivity**

A possible explanation for the correlation between N-type VDCC expression and the pattern of demyelination, may be an up-regulation of N-type VDCCs in oligodendrocytes. This could lead to an increased  $\text{Ca}^{2+}$  influx, resulting in oligodendrocyte apoptosis and disruption of the myelin sheath. However, no co-localization was seen using double immunohistochemistry for CNPase, a marker of oligodendrocytes, and  $\alpha_{1B}$ , the pore-forming subunit of N-type VDCCs, at the fluorescent microscopy level (Fig. 4.8). Therefore, we conclude that oligodendrocytes in the ON do not express N-type VDCCs.

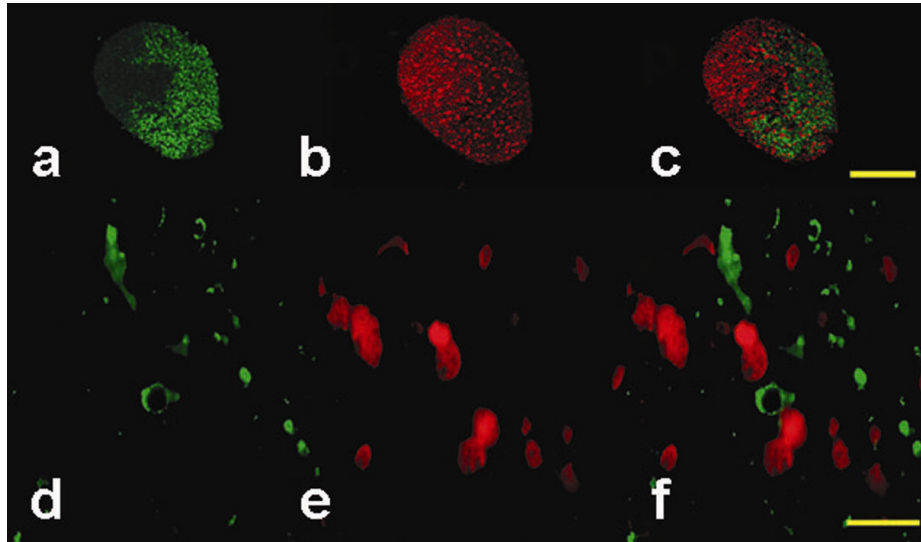


**Fig.4.8: Fluorescent microscopy co-labeling for oligodendrocytic marker (CNPase) and N-type VDCC ( $\alpha_{1B}$ )**

(a,d) CNPase immunoreactivity (b, e)  $\alpha_{1B}$  immunoreactivity (c, f) Expression of CNPase does not correlate with expression of  $\alpha_{1B}$ , as seen in the merged images. (a-c) scale bar = 100  $\mu$ m, (d-f) scale bar = 20  $\mu$ m

#### 4.7. $\omega$ -conotoxin GVIA suppresses $Ca^{2+}$ influx into the inflamed ON

In order to investigate whether  $\omega$ -conotoxin GVIA not only suppresses  $Mn^{2+}$  but also  $Ca^{2+}$  influx within the inflamed ON, we performed *in vivo*  $Ca^{2+}$  imaging in rats 15 days after immunization with MOG. Measurements of fluorescence signal intensity changes revealed an increased influx of  $Ca^{2+}$  into the ONs in rats with optic neuritis ( $166.6 \pm 20.3$ ; n=10) in comparison to healthy ONs in sham-immunized control animals ( $115.2 \pm 3.4$ ; n=6; p = 0.042) (Fig. 4.9a,b). This observation supports the hypothesis of an increased  $Ca^{2+}$  influx under inflammatory conditions and white matter injuries (Stys, 1992; Kornek, 2001).

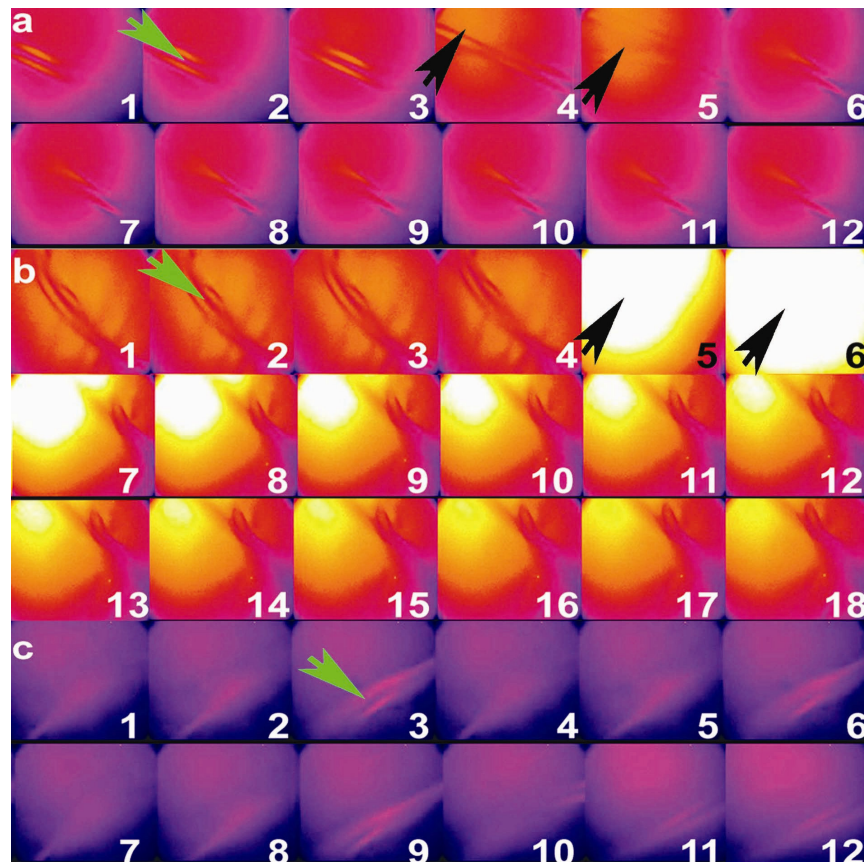


**Fig.4.9: *In vivo* calcium imaging of the rat optic nerve following KCl-induced depolarization.**

Pictures were taken every 5 seconds during a 5 min period from the time point of KCl application onwards. Each picture in the sequence represents the same part of the optic nerve. A thread (as indicated by the green arrowheads) was placed around the ON to serve as a marker ensuring the imaging of the same region. The whole sequence of images shows changes of the fluorescence signal in the 5 s intervals. The numbers indicate chronological sequence. The black arrowheads indicate start and maximum of the calcium influx seen as the increase in fluorescence intensity. (a) Sequential fluorescence microscope images, showing changes in calcium influx into the healthy optic nerve without application of any blocker. (b) Inflamed optic nerve, without blocker application, showing prominent increase in calcium-sensitive fluorescence intensity after depolarization. (c) Inflamed optic nerve treated topically with  $\omega$ -conotoxin GVIA. Note the clear reduction in calcium-sensitive fluorescence intensity after application of KCl when compared to (b).

After  $\omega$ -conotoxin GVIA was topically applied to the inflamed ONs, the depolarization-induced influx of  $\text{Ca}^{2+}$  was significantly inhibited ( $103.1 \pm 1.3$ ;  $n = 7$ )

in comparison to the control of MOG-immunized ONs ( $153.2 \pm 17.0$ ;  $n=13$ ;  $p = 0.0004$ ) (Fig. 4.10b). Treatment of healthy rats with the N-type VDCC blocker decreased the  $\text{Ca}^{2+}$  signal to a smaller extent ( $104.8 \pm 8.9$ ;  $n=4$ ) which was not significantly different to healthy ONs after topical application of normal saline ( $127.1 \pm 8.4$ ;  $n=8$ ;  $p = 0.07$ , not significant) (Fig.4.10a). During these experiments,  $\omega$ -conotoxin GVIA was applied topically in a dose of  $3 \mu\text{g}$  per ON, a dose proven to be efficient in suppressing N-type VDCC-mediated neuropathic pain in rats (Xiao, 1995).

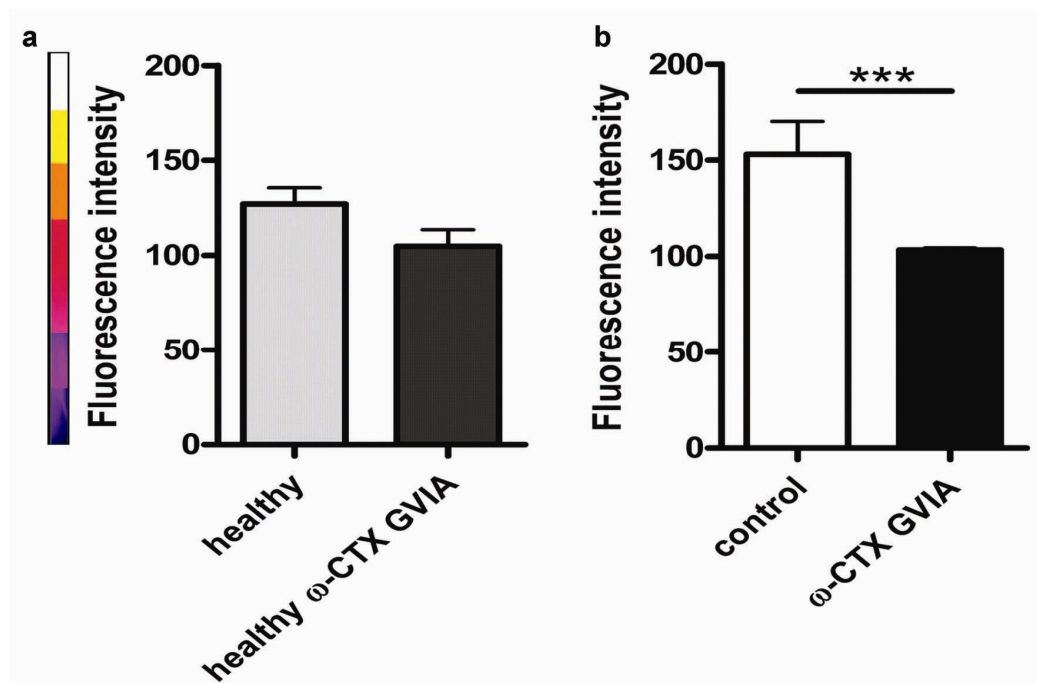


**Fig.4.10: Quantification of calcium-sensitive fluorescence intensity changes**

(a) in healthy rat optic nerves with and without application of  $\omega$ -conotoxin GVIA. (b) from rats suffering from optic neuritis with and without application of  $\omega$ -conotoxin GVIA. Application of the N-type VDCC blocker led to a highly significant reduction of fluorescence intensity. Error bars represent SEMs. \*\*\*,  $p < 0.001$ ,  $n = 13$ .

#### 4.8. Application of $\omega$ -conotoxin GVIA reduces axonal degeneration in MOG-induced optic neuritis

After we demonstrated that N-type VDCCs are up-regulated in degenerating ON axon fibers and are responsible for an increased  $\text{Ca}^{2+}$  influx into the axon, we addressed the

question of whether these phenomena play a functional role in the process of neurodegeneration. Therefore,  $\omega$ -conotoxin GVIA was continuously applied via osmotic mini-pumps to the cerebrospinal fluid of rats following MOG-immunization, and the extent of neurodegeneration was subsequently assessed by histopathology. In this context, two different treatment paradigms were compared: In the first two groups (termed “PRE”), delivery of  $\omega$ -conotoxin GVIA or vehicle was started 2 days prior to immunization. In these groups, infusion of drug or vehicle solution was continued until day 21 after immunization, corresponding to a time point 1 week after disease manifestation. In the next 2 groups (termed “LATE”), delivery of  $\omega$ -conotoxin GVIA or vehicle was started on the day of EAE onset and was continued for 1 week until day 8 of the disease. During these experiments,  $\omega$ -conotoxin GVIA was delivered at a concentration of 1.5 pmol/h with a pump rate of 0.25  $\mu$ l/h. This protocol was chosen due to results obtained from a preliminary dose-finding trial (data not shown) and according to published data describing chronic intrathecal and intracerebroventricular applications of conopeptides (Malmberg, 1995; Spampinato, 1994). All animals survived until the end of the experiment without showing obvious side effects related to  $\omega$ -conotoxin GVIA application, except for initial tremors shortly after the start of infusion. However, this effect was transient and diminished after a few days.

In the “PRE” treatment group the percentage of surviving axons within the ONs was significantly increased ( $\omega$ -conotoxin GVIA treated,  $90.4 \pm 3.7$ ,  $n=8$ ; vehicle-treated,  $47.2 \pm 8.2$ ,  $n=5$ ;  $p = 0.0016$ ) (Fig. 4.11c, f and Fig. 4.12c). In the “LATE” treatment group, a trend towards increased axonal survival was seen following treatment with  $\omega$ -conotoxin GVIA, however, this difference was not statistically significant ( $\omega$ -conotoxin GVIA treated,  $86.1 \pm 6.7$ ,  $n=8$ ; vehicle-treated,  $60.3 \pm 6.3$ ,  $n=5$ ;  $p = 0.06$ , not significant) (Fig. 4.11i, l, and Fig. 4.12 d). As far as demyelination is concerned a significant reduction was observed in both groups which received  $\omega$ -conotoxin GVIA when compared to the respective vehicle-treated control groups ( $\omega$ -conotoxin GVIA PRE treatment,  $35.9 \pm 8.7$ ,  $n=8$ ; vehicle PRE treatment,  $94.2 \pm 5.8$ ,  $n=5$ ;  $p = 0.0031$ ) (Fig. 4.11a, d and Fig. 4.12e);  $\omega$ -conotoxin GVIA LATE treatment,  $31.0 \pm 13.7$ ,  $n=8$ ; vehicle LATE treatment,  $94.5 \pm 3.2$ ,  $n=5$ ;  $p = 0.0062$ ) (Fig. 4.11g,j and Fig. 4.12f). In contrast, inflammatory infiltration within the ONs was not influenced by application of  $\omega$ -conotoxin GVIA (Fig. 4.12g, h). Furthermore, there was no effect of  $\omega$ -conotoxin GVIA on the survival of RGCs (data not shown).

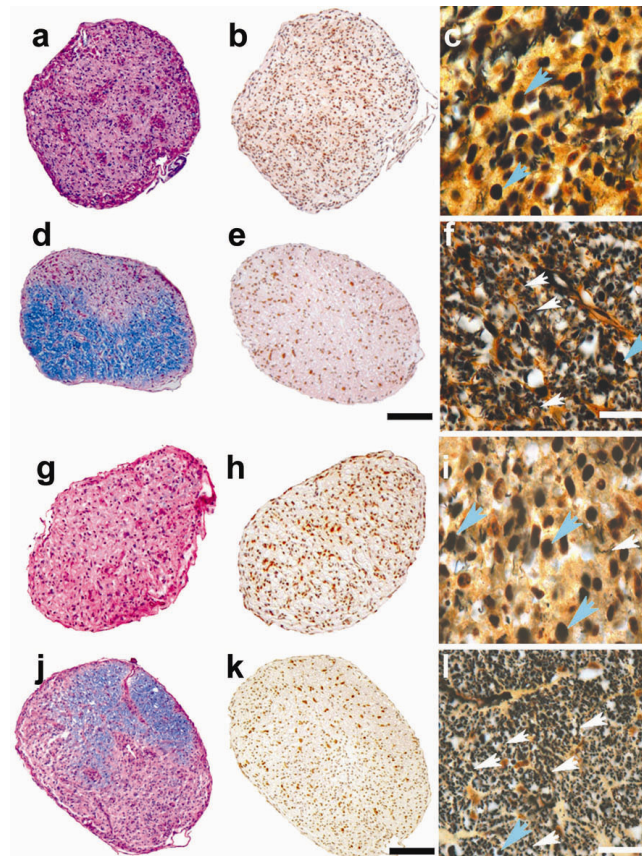


**Fig. 4.11: Effects of continuous intracerebroventricular application of  $\omega$ -conotoxin GVIA on MOG-induced optic neuritis.**

Application of vehicle (a,b, c, g,h,i) or  $\omega$ -conotoxin GVIA (d,e,f,j,k,l) was either started two days prior to immunization (a,b,c,d,e,f) or given from the day of disease onset onwards (g,h,i,j,k,l) and was continued over three weeks. (a,d,g,j): LFB staining showing the extent of demyelination (purple areas). Blue areas indicate intact myelin. Note the decreased amount of demyelination in both optic nerves treated with  $\omega$ -conotoxin GVIA (d, j). (c, f,i,l): Bielschowsky silver impregnation indicating the extent of axonal degeneration. Axons are marked by white arrowheads, green arrowheads show infiltrating macrophages. Note the low numbers of surviving axons in parallel with high numbers of macrophages in both vehicle-treated optic nerves (c, i). After treatment with  $\omega$ -conotoxin GVIA, axonal survival was improved, especially when treatment was started prior to immunization (f).

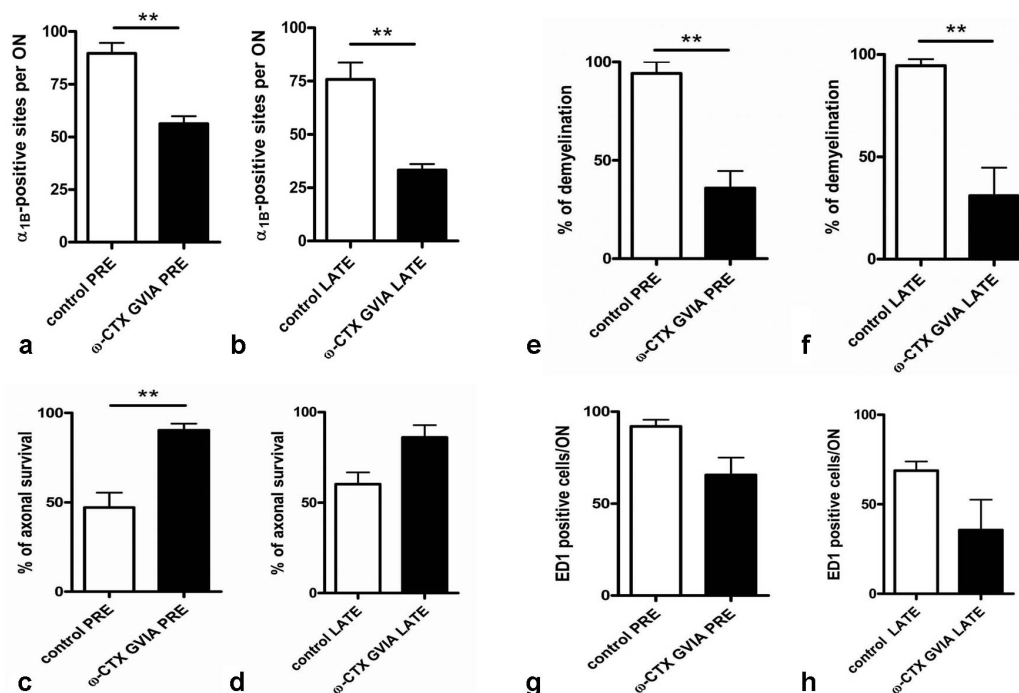


**Fig.4.12: Quantitative analyses of histological and immunohistochemical data after  $\omega$ -conotoxin GVIA treatment of MOG-induced optic neuritis**

(a, b) Quantification of  $\alpha_{1B}$ -positive sites per optic nerve after PRE treatment (a), or LATE treatment (b) with  $\omega$ -conotoxin GVIA or vehicle. (c, d), Axonal survival in the PRE (c), and the LATE (d) treatment groups. The number of surviving axons, labelled as “% of axonal survival”, is expressed as percentage of the average number of axons in the healthy optic nerve. (e, f), Extent of demyelination after application of  $\omega$ -conotoxin GVIA or vehicle according to the PRE (e) or LATE (f) treatment protocol. Demyelination is given as percentage with respect to the whole optic nerve cross-section. (g, h) Numbers of ED1-positive cells per optic nerve in the PRE (g) and the LATE treatment groups (h).

Error bars represent SEMs, \*\*,  $p < 0.01$

After quantitative analysis of  $\alpha_{1B}$  – immunoreactivity, we have observed a very significant reduction in the number of  $\alpha_{1B}$  – positive sites per optic nerve in both the PRE and LATE treatment groups. For the PRE  $\omega$ -conotoxin GVIA treated group, the average number of  $\alpha_{1B}$  – positive sites per optic nerve was  $56.2 \pm 3.6$ ,  $n = 8$  while for the vehicle treated group the average value was  $89.6 \pm 5.0$ ,  $n = 5$ ,  $p = 0.002$  (Fig. 4.12 a). For the LATE treatment, the values in the  $\omega$ -conotoxin GVIA treated group were

$33.30 \pm 2.8$ ,  $n = 5$  and in the vehicle treated  $75.8 \pm 7.9$ ,  $n = 8$ ,  $p = 0.002$ , (Fig. 4.12 b). The values are given as mean with SEM.

We also tested if  $\omega$ -conotoxin GVIA treatment affected the clinical outcome of EAE. In the pre-treatment group, the onset of disease was significantly delayed in the treated group ( $15.8 \pm 0.9$ ;  $n = 4$ ) in comparison to the control group ( $11.5 \pm 0.5$ ;  $n = 4$ ;  $p = 0.029$ ). In this case, for the clinical outcome,  $n$  signifies number of animals, not optic nerves.

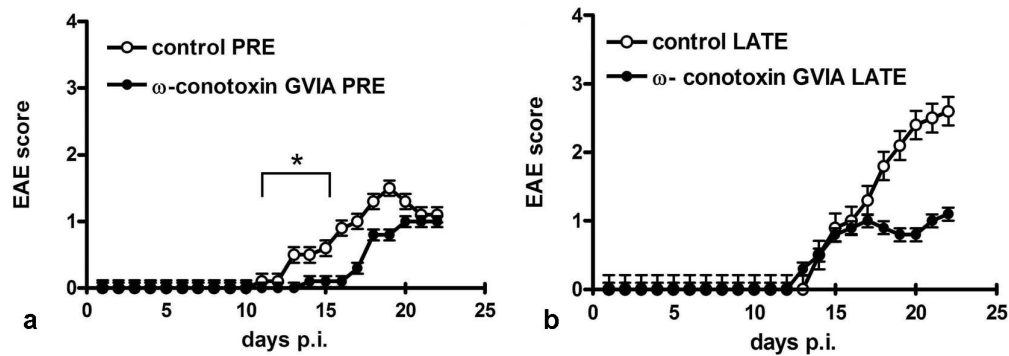


**Fig. 4.13: Score giving the severity of general neurological symptoms**

rat groups treated with  $\omega$ -conotoxin GVIA or vehicle according to the PRE (a) or LATE (b) treatment protocol. Error bars represent SEMs, \*,  $p < 0.05$

The cumulative score was significantly reduced in the  $\omega$ -conotoxin GVIA treated group ( $5.1 \pm 1.5$ ;  $n = 4$ ) in comparison to vehicle-treated control group ( $10.0 \pm 0.7$ ;  $n = 4$ ;  $p = 0.029$ ) (Fig.4.13a). In the late treatment group, however, the onset was not significantly delayed,  $12.8 \pm 0.8$  in the  $\omega$ -conotoxin GVIA treated group, ( $n = 4$ ), in comparison to the vehicle-treated group ( $14.5 \pm 1.0$ ;  $n = 4$ ; not significant). The late treatment did not improve neurological outcome in the  $\omega$ -conotoxin GVIA treated group ( $7.9 \pm 3.6$ ;  $n = 4$ ) compared to the vehicle-treated control group ( $15.0 \pm 3.0$ ;  $n = 4$ ; not significant) (Fig. 4.13b).

## 5 Discussion

### 5.1. Detection of N-type VDCC expression pattern in MOG-induced optic neuritis

This is the first study to show that an increased  $\text{Ca}^{2+}$  influx via N-type VDCCs is functionally relevant to axonal degeneration in experimental autoimmune optic neuritis. Our results, obtained by different imaging techniques, such as  $\text{Mn}^{2+}$ -enhanced MRI and *in vivo*  $\text{Ca}^{2+}$  imaging, as well as by immunohistochemistry and histopathology, suggest that N-type VDCCs are up-regulated in the inflamed optic nerve. Furthermore, we demonstrate that the expression pattern of this channel correlates with the pattern of demyelination and the distribution of  $\beta$ -APP positive axons. Our histological data are consistent with previous findings from Kornek and colleagues who observed an ectopic distribution of  $\alpha_{1B}$ , the pore-forming subunit of N-type VDCCs, in demyelinated axons, both in MS and EAE (Kornek 2001). However, these investigations were performed on brain and spinal cord tissue with no particular focus on the ON. Given that VDCCs undergo alternative splicing and have tissue-specific expression (Snutch, 1991), changes in channel distribution within the spinal cord and brain are not necessarily relevant for the inflamed ON.

Our current study gives a clear indication that not only N-type VDCCs are up-regulated in axons under pathophysiological conditions; we also show that they can be found in ON axons of healthy animals as well. In general, axonal expression of N-type VDCCs is still a matter of debate.

One of the reasons for these existing uncertainties is the fact that ON axons are too small in diameter (0.77  $\mu\text{m}$  is the mean diameter of the rat optic nerve) to allow voltage or patch-clamp studies (Oozeer, 2006). However, it is possible to investigate action potential characteristics by means of extracellular recordings which can be coupled with pharmacological explorations (Lev-Ram and Grinvald, 1986; Fern, 1995; Brown, 2000). Other techniques used to detect VDCC expression in the rat optic nerve include confocal fluorescence imaging of intracellular calcium (Sun and Chiu, 1999; Stys, 2000), immunological stainings for light, fluorescent, confocal and

electron microscopy, as well as simulations of axonal excitability (Brown, 2003; Oozeer, 2006). However, the methodology we have used for *in vivo* calcium imaging in combination with application of VDCC antagonists has been described only recently by Lingor and colleagues (manuscript in press).

*Reconciliation with previous data*

The above mentioned study performed by Sun and Chiu (Sun, 1999) focused on the fast calcium transient and examined its regulation in CNS white matter using the neonatal [postnatal day 2 (P2–P7)] rat optic nerve as a model system. This study addressed the following questions: Does the fast calcium transient originate from axons or glia and what are the axonal VDCC types that mediate this fast calcium transient? By devising dye-loading methods to label either glia or axons selectively, they showed that the fast activity-dependent calcium transients originate from axons, thus confirming the results of several previous studies (Lev-Ram and Grinvald, 1986). By further combining specific VDCC blockers with the confocal-imaging technique, they established that N-type VDCCs mediate most of the calcium transient with a smaller contribution possibly arising from R- and/or T-type calcium channels and/or reverse  $\text{Na}^+/\text{Ca}^{2+}$  exchange. P/Q- and L-type calcium channels do not seem to contribute to the calcium transient (Sun, 1999). Our results are consistent with these findings. Nevertheless, the possibility of differential VDCC expression during development should be taken into consideration. Sun and Chiu examined the neonatal rat optic nerve, while we used adult rat optic nerves in our experiments. However, currently there are no data available about age-dependent VDCC expression in the rat optic nerve. Therefore, at this point, we can conclude that N-type VDCCs are the most prominently expressed VDCC type in the rat optic nerve.

Fern and colleagues (Fern, 1995) demonstrated the presence of pharmacologically distinct VDCCs in CNS white matter (adult rat optic nerve), one sensitive to organic L-type VDCC blockers and the other sensitive to  $\omega$ -conotoxin GVIA, a specific blocker of N-type VDCCs. They also claim to have detected a species of VDCCs, sensitive to  $\omega$ -conotoxin MVIIC (a blocker of both N- and P/Q-type VDCCs) (Fern, 1995). Their results show that L-type and N-type VDCCs are involved in the development of anoxic injury in CNS white matter, since the application of the blockers of these VDCC types resulted in postanoxic CAP recovery. They claim that the third type of VDCCs, (most likely P/Q-type), influences action-potential

conduction in normoxic CNS axons (which is not the case for L- and N- type VDCCs) but does not play a role in anoxic injury.

Another interesting result from this study is the observation that N-type VDCC blockers did not have any protective effect against the development of anoxic injury when applied alone, possibly indicating a low density of N-type VDCCs compared with L-type channels (Fern, 1995). They speculate further that a number of conditions must be reached in the CNS white matter before  $\text{Ca}^{2+}$  can exert toxic influences. Thus, anoxic injury of the white matter depends on an influx of  $\text{Na}^+$  through non-inactivating  $\text{Na}^+$  channels (Stys, 1992, 1993), an influx of  $\text{Ca}^{2+}$  through N-type and L-type VDCCs, and membrane depolarization following  $\text{K}^+$  efflux (Stys, 1992). Elevated intracellular  $\text{Na}^+$  and  $\text{Ca}^{2+}$  levels together with membrane depolarization tend to reversely activate the  $\text{Na}^+/\text{Ca}^{2+}$  exchanger. This suggests that  $\text{Ca}^{2+}$  influx via VDCCs may be an initial event required for further toxic influx of  $\text{Ca}^{2+}$  via the  $\text{Na}^+/\text{Ca}^{2+}$  exchanger (Fern, 1995).

Our data confirm the assumption of a low density of N-type VDCCs in the rat optic nerve under normal physiological conditions. Using immunohistochemistry, we have detected very scarce N-type VDCC expression in healthy ONs. Furthermore, we could not detect any effect of an N-type VDCC blocker applied to the healthy nerve by *in vivo* calcium imaging. In contrast, there was a strong effect of this blocker after application on the demyelinated nerve.

Our hypothesis of an up-regulated N-type VDCC expression under autoimmune inflammatory conditions which would lead to increased  $\text{Ca}^{2+}$  influx could be reconciled with the scenario of an initial  $\text{Ca}^{2+}$  influx via VDCCs under anoxic conditions, as suggested by Fern and colleagues.

There is an increasing number of studies presenting data for converging mechanisms of anoxic/ischaemic injury of central white matter and the mechanisms of tissue damage that occur in MS (Stys, 2005). We believe that our results give an additional indication which further points in this direction.

## **5.2. Establishing functionality of the ectopically expressed N-type VDCCs**

We have extended our above described histological studies on channel expression by investigating their function. We have used *in vivo* calcium imaging coupled to topical

application of  $\omega$ -conotoxin GVIA, a specific blocker of N-type VDCCs, showing an increased  $\text{Ca}^{2+}$  influx via N-type VDCCs into the ON under autoimmune inflammatory conditions. In addition, we pharmacologically inhibited the abnormally – expressed channels, demonstrating a causal relationship between their function on the one hand and axonal degeneration on the other. The results of these experiments, acquired by the use of various techniques, indicate that the newly inserted N-type VDCCs are functional.

Passafaro and colleagues found that most of the neuronal cells contain a large intracellular pool of N-type VDCCs. These intracellular channels are present in the membrane of secretory granules and can be recruited to the cell surface (Passafaro, 1996). They further showed that the cells loaded with Fura-2 (a calcium sensitive dye) in which the channel translocation occurred, had a stronger response to depolarizing stimuli, suggesting that the newly inserted channels are functional (Passafaro, 1996). This correlates to our hypothesis of an increased  $\text{Ca}^{2+}$  influx via the newly inserted N-type VDCCs, which are recruited from an intracellular pool. We further extend this scenario to explain the robust increase of N-type VDCC expression observed in MOG-induced optic neuritis (for further details, see section 5.5).

### **5.3. Therapeutic value of $\omega$ -conotoxin GVIA, advantages and negative side-effects**

In a broader disease context, neuroprotective effects of N-type VDCC antagonists have been previously described using models of ischaemia, traumatic brain injury, and experimental neuropathic pain syndromes (Valentino, 1993; Bowersox, 1996; Burns, 1999). However, to date no studies have investigated the effects of N-type VDCC antagonists on neuronal or axonal damage under autoimmune inflammatory conditions. Many of the studies which showed neuroprotective effects of N-type VDCC antagonists in disease models other than MS have used  $\omega$ -conotoxin MVIIA (SNX-111) (Bowersox, 1996; Burns, 1999), a close structural analogue of  $\omega$ -conotoxin GVIA.  $\omega$ -conotoxin GVIA, used in our study, has a greater selectivity for N-type VDCCs than  $\omega$ -conotoxin MVIIA (Nielsen, 2000). However, the slow dissociation of  $\omega$ -conotoxin GVIA from its receptor means that it is not an ideal candidate for clinical trials due to the difficulty in controlling its local concentration

(Kristipati, 1994). Therefore,  $\omega$ -conotoxin MVIIA, which targets the same type of VDCCs and elicits similar biological effects appears to be more suitable for therapeutic implementation (Miljanich, 1995). Despite this limitation, the greater selectivity of  $\omega$ -conotoxin GVIA made it the more suitable inhibitor for determining the principle of action of N-type VDCCs in our study.

In the MRI experiments,  $\omega$ -conotoxin GVIA was applied intravenously. The most frequently reported side effect of this route of application is temporary hypotension (Bowersox, 1992). However, during the MRI measurements, a single bolus application of the drug was well tolerated in all animals. In order to reduce the risk of side effects impairing the autonomic nervous system or cardiovascular functions during the period of continuous application,  $\omega$ -conotoxin GVIA was infused via an intracerebroventricular catheter. Several studies have shown that this application route induces only small attenuations of the autonomic nervous system (Norton, 1999), except for the occurrence of a persistent tremor (Jackson, 1996). In our experimental paradigm, this effect turned out to be dose-dependent and was observed only transiently at the beginning of the infusion period.

#### **5.4. Effects of intracerebroventricular continuous infusion of $\omega$ -conotoxin GVIA on MOG-induced optic neuritis**

In our study, continuous application of  $\omega$ -conotoxin GVIA led to a very significant decrease in demyelination and increased axonal survival when therapy was started two days prior to immunization. However, although a trend towards an increase in the number of surviving axons was observed upon administration of  $\omega$ -conotoxin GVIA from the day of disease onset, this did not prove to be significant. This is in agreement with our earlier neuroprotection studies, in which application of erythropoietin, for example, exerted beneficial effects on neuronal survival only if the treatment was given according to a prophylactic paradigm (Sättler, 2004; Diem, 2005). This is explained by special characteristics of our animal model, in which first signs of neurodegeneration are detected prior to the onset of clinical symptoms (Hobom, 2004). At the time of acute disease manifestation, axonal damage within the ON had progressed (Meyer, 2001) such that therapeutic interventions targeting early pathophysiological events such as  $\text{Ca}^{2+}$  influx, are too late. Transferring this to the

human disease, in which the starting point of autoimmunity cannot be determined, neuroprotective therapies must therefore begin early and cover all subclinical periods of the disease. The application of  $\omega$ -conotoxin GVIA in our present study not only protected axons which up-regulate N-type VDCCs, but also significantly reduced demyelination within the ON. In order to investigate whether this is a primary phenomenon resulting from a blockade of N-type VDCCs possibly expressed on oligodendrocytes, we performed co-stainings of N-type VDCCs and CNPase. As an oligodendroglial expression of the channels could not be detected by these experiments, this effect might be secondary to axon protection. However, there might be an additional indirect effect via the influence of  $\omega$ -conotoxin GVIA on glutamate release. It has been suggested that  $\omega$ -conotoxin GVIA has a protective effect against focal ischemia through the inhibition of glutamate release from presynaptic sites (Takizawa, 1995). Given that glutamate excitotoxicity appears to be an important mechanism in autoimmune demyelination (Pitt, 2003), we hypothesize that the underlying mechanism of decreased demyelination after  $\omega$ -conotoxin GVIA treatment entails a reduction of glutamate excitotoxicity on oligodendrocytes.

Inflammatory infiltration appears not to be affected by  $\omega$ -conotoxin GVIA as indicated by comparable numbers of ED1-positive cells in the ONs of verum- and vehicle-treated animal groups. Furthermore, there was no effect of  $\omega$ -conotoxin GVIA on RGC survival. This might be explained by a differential expression of VDCCs in the somata and axons of these neurons. Previous studies which investigated the effect of sciatic nerve injury on somatic expression of VDCCs in rat dorsal root ganglion neurons showed a reduced expression of N-type VDCCs after axotomy (Baccei and Kocsis, 2000). Alternatively, the selective axon protection by  $\omega$ -conotoxin GVIA that we observed, could be caused by an independent pathophysiology of neuronal and axonal damage in our model. This hypothesis is supported by earlier observations showing that a proportion of RGCs die due to electrophysiological dysfunction during the induction phase of MOG-induced optic neuritis, independent of morphologically detectable ON axon fiber damage (Hobom, 2004).

### 5.5. Hypothetical mechanism of N-type VDCC up-regulation in MOG-induced optic neuritis

Explaining the mechanisms underlying the observed N-type VDCC up-regulation in demyelinated axons, we propose a hypothetical scenario which is supported by previous studies from groups who investigated metabolism and trafficking of N-type VDCCs (Sher, 1998). In these studies, a large intraneuronal pool of recruitable N-type VDCCs was observed (Passafaro, 1996), which had normal function after insertion into the axonal membrane. In our model of optic neuritis we detected a co-localization of  $\alpha_{1B}$  and  $\beta$ -APP. This suggests that disturbances of axonal transport could lead to an accumulation of vesicles containing N-type VDCCs within demyelinating axons and their insertion to the membrane. Until this point, the scenario is very similar to the one proposed by Kornek and colleagues (2001). However, considering observations made by Cavalie and colleagues (Cavalie, 1994) who detected an enhancement of calcium currents in PC12 cells after co-transfection with *c-fos* and *c-jun*, an additional mechanism could be taken into account: The expression of high-voltage activated calcium channels might be induced by immediate early genes probably at the level of transcription. This is supported by the detection of a strong immunoreactivity for *c-jun* in the cytoplasm of neurons located in subacute cerebral plaques of MS patients (Martin, 1996). In this study, the authors showed that this selective neuronal *c-jun* expression is a consistent reaction to demyelination and axonal damage. Therefore, we postulate that in parallel with the insertion of accumulated vesicles containing N-type VDCCs into the axonal membrane, immediate early genes induce new synthesis of N-type VDCCs in neurons under autoimmune inflammatory conditions. In earlier studies, we have reported increased *c-jun* immunoreactivity in 70% of RGCs after surgical transection of the optic nerve, which might further support the plausibility of this hypothesis (Hüll and Bähr, 1994).

Newly synthesized N-type VDCCs would firstly undergo a physiological sequence of events including passing from the site of synthesis through the endoplasmatic reticulum and the Golgi apparatus where they are packed into vesicles (Alberts, 1994). From here, they would normally be carried by fast axonal transport along microtubular tracks to the synaptic membrane. However, we believe that at this point

the above described mechanism starts which finally results in an insertion of the newly synthesized N-type VDCCs into the axonal membrane along the whole length of the axon and not only presynaptically located as it is under normal conditions. The insertion of both, the already existing and the newly synthesized N-type VDCCs, could be an explanation for the robust increase of channel expression which we observed in our current study. Additionally,  $\text{Ca}^{2+}$  influx via inserted channels from the pre-existing intracellular pool may affect even more intensively demyelination and axonal damage. This, in turn, might influence new synthesis of N-type VDCCs as described, creating a sort of positive feedback loop. It is beyond the scope of our current study to investigate what causes initial demyelination and disturbances of axonal transport but we mention here several observations from other groups which might clarify these issues in the context of our study. There is a number of reports about elevation of nitric oxide in multiple sclerosis (Redford, 1997) due to activation of inducible nitric oxide synthase (iNOS) in response to inflammatory stimuli occurring in MS and EAE. Many cell types including macrophages, microglia, neutrophils, express iNOS (Willenborg, 1999). Stagi and colleagues examined specifically the effect of microglial NO on axonal transport (Stagi, 2005). They describe that activated microglia and their inflammatory product NO induce a breakdown of the anterogradely directed axonal synaptic vesicle precursor transport via stimulation of *c-jun*-NH<sub>2</sub>-terminal kinase (JNK). They specifically showed that this holds true for the transport of synaptophysin and synaptotagmin, proteins which are part of the synaptic machinery and are being transported anterogradely via axonal transport. Another study by Leveque and colleagues presents data about an isolated complex in which N-type VDCCs are associated with synaptotagmin, calcium-binding protein of synaptic vesicles and syntaxin, a plasma membrane protein (Leveque, 1994). Taking into account that the vesicle precursors whose transport was obstructed by microglial NO as reported by Stagi and colleagues, contained synaptotagmin, it is not unlikely that also N-type VDCCs are localized in the same or similar vesicles. There is no study which investigated this particular matter up to date. One might speculate that under inflammatory conditions in EAE, activated microglia produce NO which induces a breakdown of axonal transport which then leads to accumulation of vesicles with precursors of various proteins, such as N-type VDCCs,  $\beta$ -APP or synaptic proteins.

## 6 Conclusions

In our study, we have addressed the subject of voltage-dependent calcium channel (VDCC) expression in the rat optic nerve during MOG-induced optic neuritis. We have focused on VDCC expression since this is a very important pathway of entry of calcium ions ( $\text{Ca}^{2+}$ ) into neurons under pathologic conditions (Stys, 2005). Our results indicate that the N-type is the major VDCC type expressed in optic nerve (ON) axon fibers in autoimmune inflammation.

Given that we have used a broad range of techniques, our data can be evaluated in different aspects.

We have combined manganese-enhanced MRI with pharmacological blocking of VDCCs in order to establish which type of VDCCs mediate manganese ( $\text{Mn}^{2+}$ ) influx into the optic nerve. In this context,  $\text{Mn}^{2+}$ , an MRI contrast agent, was used as an analog for  $\text{Ca}^{2+}$ , given that these two bivalent cations both enter neurons via VDCCs. Our results indicate that N-type VDCCs are the main gateways for  $\text{Mn}^{2+}$  entry into the ON. This observation may be of particular importance for the further implementation of manganese as an experimental MRI contrast agent.

Thus, one implication of the study affects the methodology of manganese-enhanced MRI and might promote the use of this contrast agent for the visualization of pathological CNS changes in models of autoimmune inflammation.

On the other hand, our data further elucidate the, up to date, unclear matter of VDCC expression in the rodent ON. Using immunohistochemistry for  $\alpha_{1B}$ , the pore-forming subunit of N-type VDCCs, we have detected a scarce expression of these channels in healthy optic nerves and an up-regulated expression which correlates to the pattern of demyelination in MOG-immunized optic nerves.

We have also confirmed an ectopic axonal expression of N-type VDCCs by *in vivo* calcium imaging in combination with a topically applied type-specific VDCC blocker, namely  $\omega$ -conotoxin GVIA. Given that only axons were labeled after intravitreal application of the calcium-sensitive dye, increased  $\text{Ca}^{2+}$  influx detected in MOG-immunized ONs could have originated only from the axons. These results, taken together with our histopathological data, give strong indication of an ectopic axonal expression of N-type VDCCs in MOG-induced optic neuritis. Furthermore,

these results also show the potency of conopeptides as pharmacological tools in the context of *in vivo* calcium imaging.

Another aspect to be taken into account may be the therapeutic value of N-type VDCC inhibitors. We have shown an amelioration of MOG-induced optic neuritis after continuous application of  $\omega$ -conotoxin GVIA. In this context, we have observed a very significant decrease in demyelination together with a very significant increased of axonal survival when therapy was started two days prior to immunization. Furthermore, we have detected a significant reduction of the number of  $\alpha_{1B}$ -positive sites per optic nerve in the  $\omega$ -conotoxin GVIA treated groups, following both, the early and the late treatment paradigm. This observation might indicate an improvement of the axonal transport in the treated animals (detailed explanation in 5.5.). However, there was no effect of  $\omega$ -conotoxin GVIA on the survival of retinal ganglion cells (RGCs), the neurons whose axons form the ON, as determined by counting the numbers of fluorogold-labeled cells in the retina.

Further investigations might be directed to the testing of combination therapies, which exert differential protective effects. For example, our group has previously shown that systemic application of erythropoietin (Epo) significantly increased survival and function of RGCs in MOG-induced optic neuritis (Sättler, 2004). Therefore, it is worth of examining the combined treatment of MOG-induced optic neuritis using Epo and  $\omega$ -conotoxin GVIA. Another candidate for combined therapy with  $\omega$ -conotoxin GVIA might be the Tat-Bcl-X<sub>L</sub>, the fusion protein of Bcl-X<sub>L</sub>, an anti-apoptotic member of the Bcl-2 family, and Tat, the protein transduction domain of the HIV-transactivator of transcription. The transduction of Tat-Bcl-X<sub>L</sub> in MOG-induced optic neuritis led to significant rescue of RGCs (Diem, 2005).

Our results suggest that VDCC antagonists may be beneficial in the therapy of autoimmune optic neuritis and possibly could be included in the treatment strategies for multiple sclerosis and perhaps other neurodegenerative demyelinating disorders. Possible combined therapies comprising VDCC antagonists and other known protective agents should be investigated.

However, the most important question to be addressed in the future is how to synthesize tailored  $\omega$ -conotoxins which would retain the efficacy and specificity of the native conopeptides but would have fewer adverse side-effects.

## 7 References

1. Akerman, S., Williamson, D.J. & Goadsby, P.J. Voltage-dependent calcium channels are involved in neurogenic dural vasodilatation via a presynaptic transmitter release mechanism. *Br J Pharmacol* 140, 558-66 (2003).
2. Alberts, B., Bray, D., Johnson, A., Lewis, J., Raff, M., Roberts, K. and Watson, J.D. *Molecular Biology of the Cell*, (Garland Publishing, Inc, New York and London, 1994).
3. Aoki, I., Wu, Y.J., Silva, A.C., Lynch, R.M. & Koretsky, A.P. In vivo detection of neuroarchitecture in the rodent brain using manganese-enhanced MRI. *Neuroimage* 22, 1046-59 (2004).
4. Baccei, M.L. & Kocsis, J.D. Voltage-gated calcium currents in axotomized adult rat cutaneous afferent neurons. *J Neurophysiol* 83, 2227-38 (2000).
5. Banik, N.L. Pathogenesis of myelin breakdown in demyelinating diseases: role of proteolytic enzymes. *Crit Rev Neurobiol* 6, 257-71 (1992).
6. Bean, B.P. Classes of calcium channels in vertebrate cells. *Annu Rev Physiol* 51, 367-84 (1989).
7. Bechtold, D.A., Kapoor, R. & Smith, K.J. Axonal protection using flecainide in experimental autoimmune encephalomyelitis. *Ann Neurol* 55, 607-16 (2004).
8. Bowersox, S., Mandema, J., Tarczy-Hornoch, K., Miljanich, G. & Luther, R.R. Pharmacokinetics of SNX-111, a selective N-type calcium channel blocker, in rats and cynomolgus monkeys. *Drug Metab Dispos* 25, 379-83 (1997).
9. Bowersox, S.S. & Luther, R. Pharmacotherapeutic potential of omega-conotoxin MVIIA (SNX-111), an N-type neuronal calcium channel blocker found in the venom of *Conus magus*. *Toxicon* 36, 1651-8 (1998).
10. Bowersox, S.S. et al. Cardiovascular effects of omega-conopeptides in conscious rats: mechanisms of action. *J Cardiovasc Pharmacol* 20, 756-64 (1992).
11. Bowersox, S.S. et al. Selective N-type neuronal voltage-sensitive calcium channel blocker, SNX-111, produces spinal antinociception in rat models of acute, persistent and neuropathic pain. *J Pharmacol Exp Ther* 279, 1243-9 (1996).
12. Brand-Schieber, E. & Werner, P. Calcium channel blockers ameliorate disease in a mouse model of multiple sclerosis. *Exp Neurol* 189, 5-9 (2004).

13. Brose, W.G., Gutlove, D.P., Luther, R.R., Bowersox, S.S. & McGuire, D. Use of intrathecal SNX-111, a novel, N-type, voltage-sensitive, calcium channel blocker, in the management of intractable brachial plexus avulsion pain. *Clin J Pain* 13, 256-9 (1997).
14. Brown, A.M., Westenbroek, R.E., Catterall, W.A. & Ransom, B.R. Axonal L-type  $\text{Ca}^{2+}$  channels and anoxic injury in rat CNS white matter. *J Neurophysiol* 85, 900-11 (2001).
15. Burns, L.H., Jin, Z. & Bowersox, S.S. The neuroprotective effects of intrathecal administration of the selective N-type calcium channel blocker ziconotide in a rat model of spinal ischemia. *J Vasc Surg* 30, 334-43 (1999).
16. Catterall, W.A., Perez-Reyes, E., Snutch, T.P. & Striessnig, J. International Union of Pharmacology. XLVIII. Nomenclature and structure-function relationships of voltage-gated calcium channels. *Pharmacol Rev* 57, 411-25 (2005).
17. Cavalie, A. et al. Constitutive upregulation of calcium channel currents in rat pheochromocytoma cells: role of *c-fos* and *c-jun*. *J Physiol* 479 (Pt 1), 11-27 (1994).
18. Chan, J.W. Optic neuritis in multiple sclerosis. *Ocul Immunol Inflamm* 10, 161-86 (2002).
19. Chuang, K.H. & Koretsky, A. Improved neuronal tract tracing using manganese enhanced magnetic resonance imaging with fast T(1) mapping. *Magn Reson Med* 55, 604-11 (2006).
20. Diem, R. et al. Combined therapy with methylprednisolone and erythropoietin in a model of multiple sclerosis. *Brain* 128, 375-85 (2005).
21. Diem, R. et al. HIV-Tat-mediated Bcl-X<sub>L</sub> delivery protects retinal ganglion cells during experimental autoimmune optic neuritis. *Neurobiol Dis* 20, 218-26 (2005).
22. Diem, R. et al. Methylprednisolone increases neuronal apoptosis during autoimmune CNS inflammation by inhibition of an endogenous neuroprotective pathway. *J Neurosci* 23, 6993-7000 (2003).
23. Diem, R., Sattler, M.B. & Bahr, M. Neurodegeneration and -protection in autoimmune CNS inflammation. *J Neuroimmunol* 184, 27-36 (2007).
24. Diem, R., Tschirne, A. & Bahr, M. Decreased amplitudes in multiple sclerosis patients with normal visual acuity: a VEP study. *J Clin Neurosci* 10, 67-70 (2003).

25. Ding, G. et al. Detection of BBB disruption and hemorrhage by Gd-DTPA enhanced MRI after embolic stroke in rat. *Brain Res* 1114, 195-203 (2006).
26. Doughty, S.W., Blaney, F.E., Orlek, B.S. & Richards, W.G. A molecular mechanism for toxin block in N-type calcium channels. *Protein Eng* 11, 95-9 (1998).
27. Elmslie, K.S. Calcium channel blockers in the treatment of disease. *J Neurosci Res* 75, 733-41 (2004).
28. Elmslie, K.S. Neurotransmitter modulation of neuronal calcium channels. *J Bioenerg Biomembr* 35, 477-89 (2003).
29. Fern, R., Ransom, B.R. & Waxman, S.G. Voltage-gated calcium channels in CNS white matter: role in anoxic injury. *J Neurophysiol* 74, 369-77 (1995).
30. Furukawa, T. et al. Voltage and pH dependent block of cloned N-type  $Ca^{2+}$  channels by amlodipine. *Br J Pharmacol* 121, 1136-40 (1997).
31. George, E.B., Glass, J.D. & Griffin, J.W. Axotomy-induced axonal degeneration is mediated by calcium influx through ion-specific channels. *J Neurosci* 15, 6445-52 (1995).
32. Gold, R., Linington, C. & Lassmann, H. Understanding pathogenesis and therapy of multiple sclerosis via animal models: 70 years of merits and culprits in experimental autoimmune encephalomyelitis research. *Brain* 129, 1953-71 (2006).
33. Guyton, M.K., Sribnick, E.A., Ray, S.K. & Banik, N.L. A role for calpain in optic neuritis. *Ann N Y Acad Sci* 1053, 48-54 (2005).
34. Hauser, S.L. and Oksenberg, J.R. The neurobiology of multiple sclerosis: genes, inflammation, and neurodegeneration. *Neuron* 52, 61-76 (2006).
35. Hickman, S.J., Miszkiel, K.A., Plant, G.T. & Miller, D.H. The optic nerve sheath on MRI in acute optic neuritis. *Neuroradiology* 47, 51-5 (2005).
36. Hobom, M. et al. Mechanisms and Time Course of Neuronal Degeneration in Experimental Autoimmune Encephalomyelitis. *Brain Pathology* 14, 148-157 (2004).
37. Hull, M. & Bahr, M. Regulation of immediate-early gene expression in rat retinal ganglion cells after axotomy and during regeneration through a peripheral nerve graft. *J Neurobiol* 25, 92-105 (1994).
38. Imaizumi, T., Kocsis, J.D. & Waxman, S.G. The role of voltage-gated  $Ca^{2+}$  channels in anoxic injury of spinal cord white matter. *Brain Res* 817, 84-92 (1999).

39. Jackson, H.C. & Scheideler, M.A. Behavioural and anticonvulsant effects of  $\text{Ca}^{2+}$  channel toxins in DBA/2 mice. *Psychopharmacology (Berl)* 126, 85-90 (1996).
40. Knight, R.A. et al. Acute blood-brain barrier opening in experimentally induced focal cerebral ischemia is preferentially identified by quantitative magnetization transfer imaging. *Magn Reson Med* 54, 822-32 (2005).
41. Koretsky, A.P. & Silva, A.C. Manganese-enhanced magnetic resonance imaging (MEMRI). *NMR Biomed* 17, 527-31 (2004).
42. Kornek, B. & Lassmann, H. Axonal pathology in multiple sclerosis. A historical note. *Brain Pathol* 9, 651-6 (1999).
43. Kornek, B. et al. Distribution of a calcium channel subunit in dystrophic axons in multiple sclerosis and experimental autoimmune encephalomyelitis. *Brain* 124, 1114-24 (2001).
44. Kornek, B. et al. Multiple sclerosis and chronic autoimmune encephalomyelitis: a comparative quantitative study of axonal injury in active, inactive, and remyelinated lesions. *Am J Pathol* 157, 267-76 (2000).
45. Kristipati, R. et al. Characterization of the binding of omega-conopeptides to different classes of non-L-type neuronal calcium channels. *Mol Cell Neurosci* 5, 219-28 (1994).
46. Lassmann, H. Axonal injury in multiple sclerosis. *J Neurol Neurosurg Psychiatry* 74, 695-7 (2003).
47. Lassmann, H., Raine, C.S., Antel, J. & Prineas, J.W. Immunopathology of multiple sclerosis: report on an international meeting held at the Institute of Neurology of the University of Vienna. *J Neuroimmunol* 86, 213-7 (1998).
48. Lee, J.H., Silva, A.C., Merkle, H. & Koretsky, A.P. Manganese-enhanced magnetic resonance imaging of mouse brain after systemic administration of  $\text{MnCl}_2$ : dose-dependent and temporal evolution of T1 contrast. *Magn Reson Med* 53, 640-8 (2005).
49. Leveque, C. et al. Purification of the N-type calcium channel associated with syntaxin and synaptotagmin. A complex implicated in synaptic vesicle exocytosis. *J Biol Chem* 269, 6306-12 (1994).
50. Lev-Ram, V. & Grinvald, A.  $\text{Ca}^{2+}$ - and  $\text{K}^{+}$ -dependent communication between central nervous system myelinated axons and oligodendrocytes revealed by voltage-sensitive dyes. *Proc Natl Acad Sci U S A* 83, 6651-5 (1986).

51. Lin, Y.J. & Koretsky, A.P. Manganese ion enhances T1-weighted MRI during brain activation: an approach to direct imaging of brain function. *Magn Reson Med* 38, 378-88 (1997).
52. Linington, C. et al. T cells specific for the myelin oligodendrocyte glycoprotein mediate an unusual autoimmune inflammatory response in the central nervous system. *Eur J Immunol* 23, 1364-72 (1993).
53. Linker, R.A. et al. Iron particle-enhanced visualization of inflammatory central nervous system lesions by high resolution: preliminary data in an animal model. *AJNR Am J Neuroradiol* 27, 1225-9 (2006).
54. Losseff, N.A. & Miller, D.H. Measures of brain and spinal cord atrophy in multiple sclerosis. *J Neurol Neurosurg Psychiatry* 64 Suppl 1, S102-5 (1998).
55. Lucchinetti, C. et al. Heterogeneity of multiple sclerosis lesions: implications for the pathogenesis of demyelination. *Ann Neurol* 47, 707-17 (2000).
56. Maier, K. et al. Ciliary neurotrophic factor protects retinal ganglion cells from secondary cell death during acute autoimmune optic neuritis in rats. *Brain Pathol* 14, 378-87 (2004).
57. Maier, K. et al. Effects of glatiramer acetate and interferon-beta on neurodegeneration in a model of multiple sclerosis: a comparative study. *Am J Pathol* 169, 1353-64 (2006).
58. Maier, K. et al. Multiple neuroprotective mechanisms of minocycline in autoimmune CNS inflammation. *Neurobiol Dis* 25, 514-25 (2007).
59. Malmberg, A.B. & Yaksh, T.L. Effect of continuous intrathecal infusion of omega-conopeptides, N-type calcium-channel blockers, on behavior and antinociception in the formalin and hot-plate tests in rats. *Pain* 60, 83-90 (1995).
60. Martin, G. et al. Jun expression is found in neurons located in the vicinity of subacute plaques in patients with multiple sclerosis. *Neurosci Lett* 212, 95-8 (1996).
61. McEnery, M.W. et al. Differential expression and association of calcium channel subunits in development and disease. *J Bioenerg Biomembr* 30, 409-18 (1998).
62. Merkler, D. et al. Multicontrast MRI of remyelination in the central nervous system. *NMR Biomed* 18, 395-403 (2005).
63. Meyer, R. et al. Acute neuronal apoptosis in a rat model of multiple sclerosis. *J Neurosci* 21, 6214-20 (2001).

64. Miljanich, G.P. & Ramachandran, J. Antagonists of neuronal calcium channels: structure, function, and therapeutic implications. *Annu Rev Pharmacol Toxicol* 35, 707-34 (1995).
65. Morrissey, S.P. et al. In vivo MRI and its histological correlates in acute adoptive transfer experimental allergic encephalomyelitis. Quantification of inflammation and oedema. *Brain* 119 (Pt 1), 239-48 (1996).
66. Natt, O. et al. High-resolution 3D MRI of mouse brain reveals small cerebral structures in vivo. *J Neurosci Methods* 120, 203-9 (2002).
67. Nielsen K., S.T., Lewis R. Structure-activity relationships of  $\omega$ -conotoxins at N-type voltage-sensitive calcium channels. *Journal of Molecular Recognition* 13, 55-70 (2000).
68. Nielsen, K.J., Schroeder, T. & Lewis, R. Structure-activity relationships of omega-conotoxins at N-type voltage-sensitive calcium channels. *J Mol Recognit* 13, 55-70 (2000).
69. Norton, R.S. & Olivera, B.M. Conotoxins down under. *Toxicon* 48, 780-98 (2006).
70. Norton, R.S., Paul K. Pallaghy J B. Baell C E. Wright M J. Lew J A. Angus. Polypeptide omega-conotoxin GVIA as a basis for new analgesic and neuroprotective agents. *Drug Development Research* 46, 206-218 (1999).
71. Noseworthy, J.H., Lucchinetti, C., Rodriguez, M. & Weinshenker, B.G. Multiple sclerosis. *N Engl J Med* 343, 938-52 (2000).
72. Olivera, B.M. et al. Neuronal calcium channel antagonists. Discrimination between calcium channel subtypes using omega-conotoxin from *Conus magus* venom. *Biochemistry* 26, 2086-90 (1987).
73. Oozeer, M., Veraart, C., Legat, V. & Delbeke, J. A model of the mammalian optic nerve fibre based on experimental data. *Vision Res* 46, 2513-24 (2006).
74. Passafaro, M. et al. Transient translocation of N-type calcium channels from secretory granules to the cell surface. *Ann N Y Acad Sci* 841, 119-21 (1998).
75. Passafaro, M., Rosa, P., Sala, C., Clementi, F. & Sher, E. N-type  $\text{Ca}^{2+}$  channels are present in secretory granules and are transiently translocated to the plasma membrane during regulated exocytosis. *J Biol Chem* 271, 30096-104 (1996).

76. Pautler, R.G., Silva, A.C. & Koretsky, A.P. In vivo neuronal tract tracing using manganese-enhanced magnetic resonance imaging. *Magn Reson Med* 40, 740-8 (1998).
77. Paxinos, G. and Watson, C. *The Rat Brain in Stereotaxic Coordinates*. Vol. 4th Edition (Academic Press, 1998).
78. Peterson, J.W., Bo, L., Mork, S., Chang, A. & Trapp, B.D. Transected neurites, apoptotic neurons, and reduced inflammation in cortical multiple sclerosis lesions. *Ann Neurol* 50, 389-400 (2001).
79. Pitt, D., Nagelmeier, I.E., Wilson, H.C. & Raine, C.S. Glutamate uptake by oligodendrocytes: Implications for excitotoxicity in multiple sclerosis. *Neurology* 61, 1113-20 (2003).
80. Poliak, S. & Peles, E. The local differentiation of myelinated axons at nodes of Ranvier. *Nat Rev Neurosci* 4, 968-80 (2003).
81. Raine, C.S., Cannella, B., Hauser, S.L. & Genain, C.P. Demyelination in primate autoimmune encephalomyelitis and acute multiple sclerosis lesions: a case for antigen-specific antibody mediation. *Ann Neurol* 46, 144-60 (1999).
82. Randall, A. & Benham, C.D. Recent advances in the molecular understanding of voltage-gated Ca<sup>2+</sup> channels. *Mol Cell Neurosci* 14, 255-72 (1999).
83. Ransom, B.R., Stys, P.K. & Waxman, S.G. The pathophysiology of anoxic injury in central nervous system white matter. *Stroke* 21, III52-7 (1990).
84. Rausch, M., Hiestand, P., Baumann, D., Cannet, C. & Rudin, M. MRI-based monitoring of inflammation and tissue damage in acute and chronic relapsing EAE. *Magn Reson Med* 50, 309-14 (2003).
85. Redford, E.J., Kapoor, R. & Smith, K.J. Nitric oxide donors reversibly block axonal conduction: demyelinated axons are especially susceptible. *Brain* 120 (Pt 12), 2149-57 (1997).
86. Ren, Y., Ridsdale, A., Coderre, E. & Stys, P.K. Calcium imaging in live rat optic nerve myelinated axons in vitro using confocal laser microscopy. *J Neurosci Methods* 102, 165-76 (2000).
87. Rostasy, K. et al. Tau, phospho-tau, and S-100 $\beta$  in the cerebrospinal fluid of children with multiple sclerosis. *J Child Neurol* 20, 822-5 (2005).
88. Sättler, M.B. et al. Effects of interferon-beta-1a on neuronal survival under autoimmune inflammatory conditions. *Exp Neurol* 201, 172-81 (2006).

89. Sättler, M.B. et al. Neuroprotective effects and intracellular signaling pathways of erythropoietin in a rat model of multiple sclerosis.
90. Sättler, M.B. et al. Simvastatin treatment does not protect retinal ganglion cells from degeneration in a rat model of autoimmune optic neuritis. *Exp Neurol* 193, 163-71 (2005).
91. Schellenberg, A.E., Buist, R., Yong, V.W., Del Bigio, M.R. & Peeling, J. Magnetic resonance imaging of blood-spinal cord barrier disruption in mice with experimental autoimmune encephalomyelitis. *Magn Reson Med* 58, 298-305 (2007).
92. Seeldrayers, P.A. et al. Magnetic resonance imaging investigation of blood-brain barrier damage in adoptive transfer experimental autoimmune encephalomyelitis. *J Neuroimmunol* 46, 199-206 (1993).
93. Shapira, S., Adeyemo, O.M. & Feuerstein, G. Integrated autonomic and behavioral responses to L/N  $Ca^{2+}$ -channel blocker omega-conotoxin in conscious rats. *Am J Physiol* 259, R427-38 (1990).
94. Sher, E. et al. Metabolism and trafficking of N-type voltage-operated calcium channels in neurosecretory cells. *J Bioenerg Biomembr* 30, 399-407 (1998).
95. Silva, A.C., Lee, J.H., Aoki, I. & Koretsky, A.P. Manganese-enhanced magnetic resonance imaging (MEMRI): methodological and practical considerations. *NMR Biomed* 17, 532-43 (2004).
96. Sluka, K.A. Blockade of N- and P/Q-type calcium channels reduces the secondary heat hyperalgesia induced by acute inflammation. *J Pharmacol Exp Ther* 287, 232-7 (1998).
97. Smith, T., Groom, A., Zhu, B. & Turski, L. Autoimmune encephalomyelitis ameliorated by AMPA antagonists. *Nat Med* 6, 62-6 (2000).
98. Snutch, T.P. Targeting chronic and neuropathic pain: the N-type calcium channel comes of age. *NeuroRx* 2, 662-70 (2005).
99. Snutch, T.P., Leonard, J.P., Gilbert, M.M., Lester, H.A. & Davidson, N. Rat brain expresses a heterogeneous family of calcium channels. *Proc Natl Acad Sci U S A* 87, 3391-5 (1990).
100. Snutch, T.P., Tomlinson, W.J., Leonard, J.P. & Gilbert, M.M. Distinct calcium channels are generated by alternative splicing and are differentially expressed in the mammalian CNS. *Neuron* 7, 45-57 (1991).

101. Spampinato, S. et al. Effect of omega-conotoxin and verapamil on antinociceptive, behavioural and thermoregulatory responses to opioids in the rat. *Eur J Pharmacol* 254, 229-38 (1994).
102. Stagi, M. et al. Breakdown of axonal synaptic vesicle precursor transport by microglial nitric oxide. *J Neurosci* 25, 352-62 (2005).
103. Stefferl, A. et al. Myelin oligodendrocyte glycoprotein induces experimental autoimmune encephalomyelitis in the "resistant" Brown Norway rat: disease susceptibility is determined by MHC and MHC-linked effects on the B cell response. *J Immunol* 163, 40-9 (1999).
104. Stys, P.K. & Lopachin, R.M. Mechanisms of calcium and sodium fluxes in anoxic myelinated central nervous system axons. *Neuroscience* 82, 21-32 (1998).
105. Stys, P.K. Axonal degeneration in multiple sclerosis: is it time for neuroprotective strategies? *Ann Neurol* 55, 601-3 (2004).
106. Stys, P.K. General mechanisms of axonal damage and its prevention. *J Neurol Sci* 233, 3-13 (2005).
107. Stys, P.K. White matter injury mechanisms. *Curr Mol Med* 4, 113-30 (2004).
108. Stys, P.K., Ransom, B.R., Waxman, S.G. & Davis, P.K. Role of extracellular calcium in anoxic injury of mammalian central white matter. *Proc Natl Acad Sci U S A* 87, 4212-6 (1990).
109. Stys, P.K., Waxman, S.G. & Ransom, B.R. Ionic mechanisms of anoxic injury in mammalian CNS white matter: role of Na<sup>+</sup> channels and Na<sup>+</sup>-Ca<sup>2+</sup> exchanger. *J Neurosci* 12, 430-9 (1992).
110. Sun, B.B. & Chiu, S.Y. N-type calcium channels and their regulation by GABAB receptors in axons of neonatal rat optic nerve. *J Neurosci* 19, 5185-94 (1999).
111. Takizawa, S. et al. A selective N-type calcium channel antagonist reduces extracellular glutamate release and infarct volume in focal cerebral ischemia. *J Cereb Blood Flow Metab* 15, 611-8 (1995).
112. Terlau, H. & Olivera, B.M. Conus venoms: a rich source of novel ion channel-targeted peptides. *Physiol Rev* 84, 41-68 (2004).
113. Trapp, B.D., Ransohoff, R. & Rudick, R. Axonal pathology in multiple sclerosis: relationship to neurologic disability. *Curr Opin Neurol* 12, 295-302 (1999).

114. Turner, R.J., Van den Heuvel, C. & Vink, R. Amiloride increases neuronal damage after traumatic brain injury in rats. *J Am Coll Nutr* 23, 534S-537S (2004).
115. Valentino, K. et al. A selective N-type calcium channel antagonist protects against neuronal loss after global cerebral ischemia. *Proc Natl Acad Sci U S A* 90, 7894-7 (1993).
116. Walter, S. et al. The LPS receptor, CD14, in experimental autoimmune encephalomyelitis and multiple sclerosis. *Cell Physiol Biochem* 17, 167-72 (2006).
117. Watanabe, T. et al. In vivo 3D MRI staining of the mouse hippocampal system using intracerebral injection of  $MnCl_2$ . *Neuroimage* 22, 860-7 (2004).
118. Watanabe, T., Frahm, J. & Michaelis, T. Functional mapping of neural pathways in rodent brain in vivo using manganese-enhanced three-dimensional magnetic resonance imaging. *NMR Biomed* 17, 554-68 (2004).
119. Watanabe, T., Michaelis, T. & Frahm, J. Mapping of retinal projections in the living rat using high-resolution 3D gradient-echo MRI with  $Mn^{2+}$ -induced contrast. *Magn Reson Med* 46, 424-9 (2001).
120. Watanabe, T., Radulovic, J., Boretius, S., Frahm, J. & Michaelis, T. Mapping of the habenulo-interpeduncular pathway in living mice using manganese-enhanced 3D MRI. *Magn Reson Imaging* 24, 209-15 (2006).
121. Waxman, S.G. & Ritchie, J.M. Molecular dissection of the myelinated axon. *Ann Neurol* 33, 121-36 (1993).
122. Waxman, S.G. Demyelination in spinal cord injury and multiple sclerosis: what can we do to enhance functional recovery? *J Neurotrauma* 9 Suppl 1, S105-17 (1992).
123. Waxman, S.G., Black, J.A., Ransom, B.R. & Stys, P.K. Anoxic injury of rat optic nerve: ultrastructural evidence for coupling between  $Na^+$  influx and  $Ca^{2+}$ -mediated injury in myelinated CNS axons. *Brain Res* 644, 197-204 (1994).
124. Weissert, R. et al. MHC haplotype-dependent regulation of MOG-induced EAE in rats. *J Clin Invest* 102, 1265-73 (1998).
125. Wekerle, H., Kojima, K., Lannes-Vieira, J., Lassmann, H. & Linington, C. Animal models. *Ann Neurol* 36 Suppl, S47-53 (1994).
126. Westenbroek, R.E. et al. Biochemical properties and subcellular distribution of an N-type calcium channel alpha 1 subunit. *Neuron* 9, 1099-115 (1992).

127. Willenborg, D.O., Staykova, M.A. & Cowden, W.B. Our shifting understanding of the role of nitric oxide in autoimmune encephalomyelitis: a review. *J Neuroimmunol* 100, 21-35 (1999).
128. Xiao, W.H. & Bennett, G.J. Synthetic omega-conopeptides applied to the site of nerve injury suppress neuropathic pains in rats. *J Pharmacol Exp Ther* 274, 666-72 (1995).
129. Zamponi, G. *Voltage-Gated Calcium Channels*, (Landes Bioscience, Kluwer Academic, Georgetown, New York, 2005).
130. Zivadinov, R. & Sepcic, J. [Use of magnetic resonance imaging in the diagnosis and prognosis of multiple sclerosis]. *Lijec Vjesn* 128, 295-308 (2006).

## List of tables and figures

### TABLES

Table 1: Classification of MS types and current treatments	10
Table 2: Summary of pathologies and putative mechanisms of different patterns of demyelination in MS	13
Table 3: Detailed overview of the localization and cellular functions of different VDCC types	20
Table 4: Summary of nomenclature and pharmacology of VDCCs	21

### FIGURES

Fig.2.1: Possible mechanisms of injury and repair in multiple sclerosis	12
Fig.2.2: Events initiated during acute injury of CNS white matter	16
Fig.2.3: Schematic representations of VDCC structure and possible combinations of different subunits	22
Fig.3.1: Position of the animal in the holder used for placing in the MR scanner	34
Fig.3.2: Selected regions of interest (ROIs) used in analysis of MR images	35
Fig.4.1: T1-weighted MR images of optic nerves	38
Fig.4.2: T1-weighted MR images obtained 10 min after $Mn^{2+}$ application demonstrating the effects of type-specific VDCC blockers and an AMPA-receptor inhibitor on the $Mn^{2+}$ -induced enhancement within the inflamed ONs	40
Fig.4.3: T1-weighted MR images showing the effects of type-specific HVA VDCC blockers on $Mn^{2+}$ -induced enhancement within the inflamed optic nerves	41
Fig.4.4: Expression of N-type VDCCs in rat optic nerve during optic neuritis, compared to myelin-specific histopathological staining (LFB)	43
Fig.4.5: Quantitative analysis of $\alpha_{1B}$ immunoreactivity and	

comparison to axonal survival and demyelination	45
Fig.4.6: Fluorescent microscopy co-labeling for axonal marker ( $\beta$ -APP) and N-type VDCC ( $\alpha_{1B}$ )	46
Fig.4.7: Fluorescent microscopy co-labeling for astrocytic marker (GFAP) and N-type VDCCs ( $\alpha_{1B}$ )	47
Fig.4.8: Fluorescent microscopy co-labeling for oligodendrocytic marker (CNPase) and N-type VDCC ( $\alpha_{1B}$ )	48
Fig.4.9: <i>In vivo</i> calcium imaging of the rat optic nerve following KCl-induced depolarization	49
Fig.4.10: Quantification of calcium-sensitive fluorescence intensity changes	50
Fig.4.11: Effects of continuous intracerebroventricular application of $\omega$ -conotoxin GVIA on MOG-induced optic neuritis	52
Fig.4.12: Quantitative analyses of histological and immunohistochemical data after $\omega$ -conotoxin GVIA treatment of MOG-induced optic neuritis	53
Fig. 4.13: Score giving the severity of general neurological symptoms	54

## APPENDIX 1: Abbreviations

aCSF	artificial Cerebrospinal Fluid
AIDS	Acquired Immune Deficiency Syndrom
AMPA	alpha-Amino-3-hydroxy-5-Methyl-4-isoxazolePropionic Acid
APP	Amyloid Precursor Protein
BBB	Blood Brain Barrier
Bcl-X <sub>L</sub>	anti-apoptotic member of the <i>B-cell lymphoma</i> gene family
BN	Brown Norway rat strain
CAP	Compound Action Potential
CFA	Complete Freund's Adjuvant
CNPase	2', 3'-cyclic nucleotide 3'-phosphodiesterase
CNS	Central Nervous System
CTLA-4	Cytotoxic T-lymphocyte-associated protein 4
DAB	Diaminobenzidin
DAPI	4', 6-diamidino-2-phenylindole
EAE	Experimental Autoimmune Encephalomyelitis
Epo	Erythropoietin
EtOH	Ethanol
FLASH MRI	Fast Low Angle Shot Magnetic Resonance Imaging
GFAP	Glial Fibrillary Acidic Protein
HIV	Human Immunodeficiency Virus
HVA	High Voltage Activated
ICAM-1	Intercellular Adhesion Molecule 1
IEG	Immediate Early Genes
IHC	Immunohistochemistry
iNOS	inducible Nitric Oxide Synthase
IP3	Inositol triphosphate
IVA	Intermediate Voltage Activated
JNK	<i>c-jun</i> -NH <sub>2</sub> -terminal kinase
LVA	Low Voltage Activated
MHC	Major-Histocompatibility-Complex
MOG	Myelin Oligodendrocyte Glycoprotein
MRI	Magnetic Resonance Imaging

MS	Multiple Sclerosis
NO	Nitric Oxide
OG	Oligodendrocytes
OGB	Oregon Green BAPTA
ON	Optic Nerve
PBS	Phosphate Buffer Saline
PC12	Phaeochromocytoma Cells clone 12
PFA	Paraformaldehyde
PX2	ATP-gated ion channel, subtype 3
RGC	Retinal Ganglion Cells
ROI	Region Of Interest
RT	Room Temperature
SI	Signal Intensity
Tat	HIV-transactivator of transcription
TCR	T-Cell Receptor
Th	T helper cells
TNF- $\alpha$	Tumor Necrosis Factor- $\alpha$
TR	Repetition Time
TE	Echo Time
VCAM-1	Vascular-Cell Adhesion Molecule 1
VDCC	Voltage-Dependent Calcium Channels

## APPENDIX 2: CV

### IVANA GADJANSKI

#### *Curriculum vitae*

- DATE AND PLACE OF BIRTH: 10 September 1979. Novi Sad, Serbia
- CURRENT ADDRESS: Christophorusweg Str. 14, 37075, Göttingen, Germany
- HOME ADDRESS: Mihaila Bogicevica Str. 6, 11000 Belgrade, Serbia
- PHONE: +49 551 9953553
- CELL PHONE: +49 176 235 15 774
- E-MAIL: igadjan@gwdg.de, igadjanski@gmail.com
- MARITAL STATUS: single
- EDUCATION:
  - 1994-1998: III Belgrade Gymnasium, Belgrade, Serbia (biology orientation); Evaluation: 60/60 (A+)
  - 1998-2003: Bachelor of Science, Faculty of Biology at Belgrade University. Average mark 9.7 out of 10 and Final Exam Paper mark 10 out of 10 (Title: Therapeutic Effect of Combined Application of Ribavirin and Tiazofurin in Treatment of Experimental Autoimmune Encephalomyelitis in EAE-sensitive Dark Agouti Rats)
  - 2003-2006: Postgraduate studies, Faculty of Biology, Department of Neurobiology and Immunology at Institute for Biological Research “Sinisa Stankovic” Belgrade
  - 2004-until present: Doctoral studies, Georg-August-Universität, Faculty of Biology and University Clinic, Dept. Neurology, Göttingen, Germany. Focus on pathologic mechanisms occurring under autoimmune inflammatory conditions in animal model of multiple sclerosis.
- PUBLICATIONS:
  - Diem R., Taheri N., Dietz G., Kuhnert A., Maier K., Sättler MB., **Gadjanski I.**, Merkler D. and Bähr M.: HIV-Tat-mediated Bcl-XL

delivery protects retinal ganglion cells during experimental autoimmune optic neuritis, *Neurobiol Dis.* 2005 Nov;20(2):218-26.

- Sättler MB, Demmer I, Williams SK, Maier K, Merkler D, **Gadjanski I**, Stadelmann C, Bahr M, Diem R. Effects of interferon-beta-1a on neuronal survival under autoimmune inflammatory conditions. *Exp Neurol.* 2006 Sep;201(1):172-81.
- Boretius S, **Gadjanski I**, Demmer I, Diem R, Frahm J MRI of optic neuritis in a rat model *submitted*
- Lingor P, Knöferle J, **Gadjanski I**, Diem R. Bähr M *manuscript in preparation*
- **Gadjanski I**, Boretius S, Lingor P, Knöferle J, Sättler MB, Williams SK, Sühs KW, Michaelis T, Frahm J, Bähr M, Diem R. Axon degeneration in autoimmune optic neuritis depends on the N-type of voltage gated calcium channels *manuscript submitted*
- POSTERS and ORAL PRESENTATIONS:
  - Student talk on MRI in optic neuritis, NeuroNE (Network of Excellence) Workshop: *Imaging in Neuroscience*, Service Hospitalier Frédéric Joliot, Orsay, France, Oct 2005
  - Results of the study conducted by I.G. presented by Dr. Ricarda Diem, supervisor of the project, as the lecture in Session Mechanisms of damage to axons and myelin, 22<sup>nd</sup> Congress of the European Committee for the Treatment and Research in Multiple Sclerosis (ECTRIMS), 27-30 Sep 2006, Madrid, Spain
  - Poster presentation at *Neuroscience 2006*, Congress of Society of Neuroscience, Atlanta, USA, Oct 2006
  - Poster presentation at 31<sup>st</sup> Göttingen Neurobiology Conference & 7<sup>th</sup> Meeting of the German Neuroscience Society, 29th Mar-1<sup>st</sup> April 2007, Goettingen, Germany
  - Student talk at the Brain Repair Centre Spring school, Cambridge University, April 2007, Cambridge, UK

- WORK EXPERIENCE:

- Technical practice at the Institute for Physiology of Nutrition, Faculty of Natural Sciences and Mathematics, Potsdam University, Germany (IAESTE Stipend), Aug-Sep 2001
- Columnist in several Serbian magazines for popularization of science, 2001-2005
- Translator of books for popularization of science, from english to serbian (e.g. Susan Greenfield: The Human Brain)
- LAB EXPERIENCE
  - Immunohistochemistry
  - Histopathological stainings
  - Western blotting
  - ELISA
  - stereotactic operations
  - various methods of tissue isolation in CNS
  - animal MRI (Bruker system)
  - osmotic pump and brain infusion system implantation
  - animal OCT (optical coherence tomography)
- COMPUTER KNOWLEDGE:
  - Operating systems: Windows, Linux SuSe
  - Software: Microsoft Office (full package), Photoshop CS2, Adobe Illustrator
  - Languages: HTML (elements)
- METHODOLOGY COURSES
  - EMBO School of Biophysics “Ettore Majorana” Center, May 2005, Erice, Sicily
  - Neurobiology of Disease Workshop: Motor Neuron Diseases, *Neuroscience 2006*, SfN Congress, Oct 2006, Atlanta, USA
  - SFN Short Course: Confocal Microscopy & Stereology, *Neuroscience 2006*, SfN Congress, Oct 2006, Atlanta, USA
  - Course for Experimental Microsurgical Techniques and Radiotelemetry in International Microsurgical Training Centre (prof. Renée Remie and prof. Klaas Kramer), Lelystad, Netherlands

- Course: Foundations of quantitative imaging and data analysis, ISMRM (International Society for Magnetic Resonance in Medicine) congress, May 2007, Berlin
- Course: MR Physics and Techniques for Clinicians, ISMRM (International Society for Magnetic Resonance in Medicine) congress, May 2007, Berlin
- AWARDS:
  - Scholarship of the Norwegian Government: *For the Promising Generation*, Oct 2001
  - Scholarship of the Karadjordjevic Royal Family Fund, Feb 2002
  - Scholarship of the Foundation for Supporting Young Talents, Republic of Serbia, 2001-2003
  - Scholarship of the Ministry of Science, Technology and Development, Republic of Serbia, 2004
  - Certificate of Excellence, University of Belgrade, 2004
  - Partecipance Grant from EMBO School of Biophysics “Ettore Majorana” Center Erice, Sicily, May 2005
  - Scholarship for postdoctoral studies of the Ministry of Science, Technology and Development, Republic of Serbia, 2006
  - New Entry Stipend from International Society of Magnetic Resonance in Medicine, May 2007

## Acknowledgements

I would like to thank Dr. Ricarda Diem, for being an extraordinary supervisor and a good friend. I am thankful to Dr. Mathias Bähr for giving me the opportunity to work in this great lab. Everybody in the lab had some positive effect on the preparation of this PhD thesis. Barbara Müller, Nadine Meyer, Ina Boger, Sarah Williams, Muriel Sättler, Jens Pehlke, Wolfram Sühs, Katharina Maier, Sönke Schwarting, Thorsten Döppner, Payam Dibaj, Christian Rau, Hannes Vossfeldt, Jana Zschüntsich, Mimount El Aanbouri and all the others, made everything much more pleasant. The numerous cups of coffee we have been drinking together had very good effect on the working ability.

I appreciate very much the opportunity of being able to work in the very inspiring environment of the group NMR in Biomedicine in Max Planck Institute for biophysical chemistry under supervision of Dr. Jens Frahm, Dr. Susann Boretius and Dr. Thomas Michaelis. I really enjoyed working with Henry Lütcke, Matthias Küntzel, Michael Schütte and Alireza Abaei. And, very important as well is the fact that the coffee machine is also great there.

Many thanks to great people in the lab in Waldweg, Manuel Garrido, Veronique Planchamp, Ligia Ferreira, Johanna Knöferle, Jan Koch, Paul Lingor and all the others for being not only great to have discussions with but also to have a cup of coffee together.

I am also thankful to Anjana Nityanandam for being such a good friend (and for her permanent will to join me whenever I needed a cup of coffee and conversation).

I would like to express my enormous gratitude to my parents, Ksenija Maricki Gadjanski and Ivan Gadjanski, for their love and support. I am also grateful to Ana and little Luka and to all of my friends for being there for me, always.

Желела бих и посебно да се захвалим својим родитељима на љубави и подршци коју су ми пружили. Велико хвала и Ани и малом Луки, зато што постоје.

Хвала свим мојим пријатељима који су несебично и неуморно били ту за мене.

Увек.

*There is no doubt that the human mind is fundamentally incapable of solving these formidable problems (the origin of life, nature of matter, origin of movement, and appearance of consciousness). Our brain is an organ of action that is directed toward practical tasks; it does not appear to have been built for discovering the ultimate causes of things, but rather for determining their immediate causes and invariant relationships. And whereas this may appear to be very little, it is in fact a great deal. Having been granted the immense advantage of participating in the unfolding of our world, and of modifying it to life's advantage, we may proceed quite nicely without knowing the essence of things.*

*Advice for a young investigator*

**Santiago Ramón y Cajal**